

STUDY OF SOLID OXIDE FUEL CELL INTERCONNECTS,  
PROTECTIVE COATINGS AND ADVANCED PHYSICAL  
VAPOR DEPOSITION TECHNIQUES

by

Paul Edward Gannon

A dissertation submitted in partial fulfillment  
of the requirements for the degree

of

Doctor of Philosophy

in

Engineering

MONTANA STATE UNIVERSITY  
Bozeman, Montana

January 2007

©COPYRIGHT

by

Paul Edward Gannon

2007

All Rights Reserved

APPROVAL

of a dissertation submitted by

Paul Edward Gannon

This dissertation had been read by each member of the dissertation committee and has been found to be satisfactory regarding content, English usage, format, citations, bibliographic style, and consistency, and is ready for submission to the Division of Graduate Education.

Dr. Max Deibert  
Committee Chair

Approved for the Department of Chemical and Biological Engineering

Dr. Ronald Larsen  
Department Head

Approved for the Division of Graduate Education

Dr. Carl A Fox  
Vice Provost

### STATEMENT OF PERMISSION TO USE

In presenting this dissertation in partial fulfillment of the requirements for a doctoral degree at Montana State University, I agree that the Library shall make it available to borrowers under rules of the Library. I further agree that copying of this dissertation is allowable only for scholarly purposes, consistent with "fair use" as prescribed in the U.S. Copyright Law. Requests for extensive copying or reproduction of this dissertation should be referred to ProQuest Information and Learning, 300 North Zeeb Road, Ann Arbor, Michigan 48106, to whom I have granted "the exclusive right to reproduce and distribute my dissertation in and from microform along with the non-exclusive right to reproduce and distribute my abstract in any format in whole or in part."

Paul Edward Gannon

January, 2007

## ACKNOWLEDGEMENTS

I am indebted to many people for making this unique and challenging graduate school experience extremely enjoyable and rewarding. Special thanks to my advisor and committee members, Drs. Max Deibert, Vladimir Gorokhovsky, Richard Smith, Zhengou (Gary) Yang, and Mark Young for excellent guidance throughout the graduate program, academically and otherwise. It was a great pleasure working with and learning from my advisor and committee members, in addition to several other outstanding professors, staff and student colleagues at MSU. Attending numerous external conferences permitted a remarkable opportunity to establish fruitful relationships with exceptional scientists, engineers and business professionals from around the world. I am very grateful for the dedicated people behind the high temperature electrochemistry center (HiTEC) who made this experience possible. I would also like to extend my sincere appreciation for continuous support from countless family and friends.

## TABLE OF CONTENTS

LIST OF FIGURES .....	vii
LIST OF TABLES.....	x
ABSTRACT.....	xi
1. INTRODUCTION .....	1
Dissertation Overview .....	2
Solid Oxide Fuel Cell (SOFC) Technology.....	2
Historical Perspectives.....	5
Recent Development.....	7
Planar SOFC(IC) Development .....	8
Functional Requirements .....	8
Ceramic Materials.....	10
Metallic Alloys.....	10
Investigation Purpose, Significance and Limitations.....	12
Definition Of Terms.....	12
2. SOFC METALLIC INTERCONNECT DEGRADATION.....	14
Metal Alloy Corrosion at High-temperatures .....	14
Thermodynamics.....	15
Kinetics .....	20
Degradation Mechanisms.....	25
Protective Coatings and Example Applications.....	28
Conventional Protective Coating Deposition Techniques .....	29
3. ADVANCED COATING TECHNOLOGY FOR SOFC(IC) PROTECTION .....	31
Overview .....	31
Physical Vapor Deposition Technology .....	31
SOFC(IC) Coating Structures .....	33
Research Methods .....	34
Metallic Alloy Substrates and Surface Finishes .....	35
Arcomac Surface Engineering Facilities and Technology.....	36
MSU Evaluation Facilities .....	39
Collaborator Evaluation Facilities .....	40

## TABLE OF CONTENTS - CONTINUED

4. INVESTIGATION RESULTS, OBSERVATIONS AND DISCUSSIONS .....	41
Overview.....	41
SOFC Interconnect-Relevant Performance.....	43
Surface Oxidation Behavior.....	44
Uncoated Specimens.....	44
Coated Specimens.....	47
Area Specific Resistance.....	59
Cr Volatility .....	64
5. CONCLUSIONS.....	69
Summary Of Results .....	69
Considerations for Future Work .....	70
REFERENCES CITED.....	74

## LIST OF FIGURES

Figure	Page
1.1. SOFC schematics: a) with associated reactions; b) planar repeat unit design [8].....	3
1.2. Example of 5x5 cell “window pane-style” SOFC stack 175kW scale-up design [4].....	4
1.3. Examples of a) planar; b) sealless tubular; and, c) segmented-in-series SOFC designs.....	7
1.4. Fe/Cr/Ni ternary phase diagram [14].....	11
2.1. Schematic illustration of high temperature metal oxidation reactions and transport processes for two scenarios: a) oxygen anion transport dominant; and b) metal cation transport dominant.....	22
3.1. SOFC(IC) advanced PVD coating designs.....	34
3.2. 430SS substrate plate (~100 x 100 x 1mm) with laser cut specimen tabs: a) uncoated; b) with 0.5-1.5 $\mu$ m LAFAD TiCoMnCrAlYO coating.....	36
3.3. Schematic illustration of Arcomac’s large area filtered arc deposition (LAFAD) surface engineering system.....	37
3.4. Schematic side view of hybrid FA-EBPVD process.....	38
4.1. Crofer 22APU (lap/polished surface); before (a) and, after (b) 2,000 hours in 800°C air.....	45
4.2. EDS elemental map of TGO scale formed on Crofer 22APU after ~750hours in 800°C air.....	45
4.3. SEM images of spontaneous spallation of TGO scale grown on Crofer 22APU after 2,000 hours oxidation in 800°C air: (a) secondary electron image; (b) backscattered electron image providing contrast between metal (bright) and oxide (dark).....	46
4.4. SEM cross section image of 430SS after ~1,000 hours ASR testing in 800°C air.....	47

## LIST OF FIGURES – CONTINUED

Figure	Page
4.5. ~1 $\mu\text{m}$ FA-EBPVD $(\text{Co},\text{Mn})_3\text{O}_4$ coating on 430SS before and after ~100 hours in 800°C air.....	48
4.6. GI-XRD patterns for the ~1.0 $\mu\text{m}$ FA-EBPVD $(\text{Mn},\text{Co})_3\text{O}_4$ coating on 430SS: a) as-deposited; b) subsequent 100 hours oxidation in air at 800°C.....	49
4.7. Cross section EDS elemental maps of ~1.0 $\mu\text{m}$ FA-EBPVD $(\text{Co},\text{Mn})_3\text{O}_4$ after: a) ~100; b) ~450; and, c) ~700 hours in 800°C air; and, d) plot of estimated TGO scale thickness as a function of time.....	50
4.8. SEM images and corresponding EDS elemental mappings from a ~2.0 $\mu\text{m}$ LAFAD AlCrYO bottom layer coating with ~1.0 $\mu\text{m}$ FA-EBPVD $(\text{Co},\text{Mn})_3\text{O}_4$ coating on 430SS before and after ~300 hours in 800°C air.....	52
4.9. SEM images and corresponding EDS elemental mappings from a ~0.3 $\mu\text{m}$ LAFAD AlCrYO bottom layer coating with ~1.0 $\mu\text{m}$ FA-EBPVD $(\text{Co},\text{Mn})_3\text{O}_4$ coating on 430SS before and after ~300 hours in 800°C air.....	53
4.10. SEM surface images of uncoated and (~2.0 $\mu\text{m}$ LAFAD TiCrAlYO) coated 430SS.....	54
4.11. SEM surface images of ~2.0 $\mu\text{m}$ LAFAD TiCrAlYO coated 430SS before and after ~1,200 hours in 800°C air.....	55
4.12. SEM images of ~2 $\mu\text{m}$ LAFAD TiCrAlYO coated 430SS amorphous/nano-crystalline coating regions before and after 1,200 hours in 800°C air.....	55
4.13. SEM images with EBSD Kikuchi SAED patterns of a ~2.0 $\mu\text{m}$ LAFAD TiCrAlYO coating before and after ~1,200 hours in 800°C air.....	56
4.14. Schematic illustration of surface finish and influence on coating evolution during high temperature oxidizing exposures.....	57
4.15. Cross section SEM image with overlaying EDS elemental linescan from a ~2 $\mu\text{m}$ LAFAD TiCrAlYO coating after ~1,200 hours in 800C air: a) at roll mark area; b) at smooth surface area.....	58

## LIST OF FIGURES – CONTINUED

Figure	Page
4.16. Summary ASR data from Crofer 22 APU with and without coatings, in 800°C air.....	60
4.17. Summary ASR data from 430SS with and without coatings, in 800°C air.....	62
4.18. Cr volatility measurements (LBNL) from coated (FA-EBPVD (Co,Mn) <sub>3</sub> O <sub>4</sub> ) and uncoated 430SS.....	64
4.19. SEM image and EDS elemental mapping of specimen surface near breakaway tab area showing coating removal and substrate exposure....	65
4.20. Cr volatility measurements (MSU) from coated (LAFAD TiCrAlYO) and uncoated 430SS.....	66
4.21. Calculated thermodynamic equilibrium vapor pressures of Cr species (in moist air 800C air) above LAFAD TiCrAlYO coating.....	68
5.1. TEM image of LAFAD CrN(CrN/AlN) layered coating on 304 steel....	71

## LIST OF TABLES

Table		Page
2.1.	Kröger-Vink notation for point defects in crystals.....	19
4.1.	LAFAD process targets: a) with reactive gas combinations; O, N and M represent processes using oxygen, nitrogen and an oxygen/nitrogen mix respectively, blank cells represent target combinations not yet explored; b) compositions (wt%).....	41
4.2.	Table 4.2. LAFAD and FA-EBPVD coatings; a) single segment LAFAD coating compositions, b) single segment FA-EBPVD coating composition and, c) two segment LAFAD + FA-EBPVD coatings.....	42
4.3.	Ferritic alloys used in this study (estimated compositions in wt%).....	43

## ABSTRACT

High energy conversion efficiency, decreased environmentally-sensitive emissions and fuel flexibility have attracted increasing attention toward solid oxide fuel cell (SOFC) systems for stationary, transportation and portable power generation. Critical durability and cost issues, however, continue to impede wide-spread deployment. Many intermediate temperature (600-800°C) planar SOFC systems employ metallic alloy interconnect components, which physically connect individual fuel cells into electric series, facilitate gas distribution to appropriate SOFC electrode chambers (fuel/anode and oxidant[air]/cathode) and provide SOFC stack mechanical support. These demanding multifunctional requirements challenge commercially-available and inexpensive metallic alloys due to corrosion and related effects.

Many ongoing investigations are aimed at enabling inexpensive metallic alloys (via bulk and/or surface modifications) as SOFC interconnects (SOFC(IC)s). In this study, two advanced physical vapor deposition (PVD) techniques: large area filtered vacuum arc deposition (LAFAD), and filtered arc plasma-assisted electron beam PVD (FA-EBPVD) were used to deposit a wide-variety of protective nanocomposite (amorphous/nanocrystalline) ceramic thin-film ( $<5\mu\text{m}$ ) coatings on commercial and specialty stainless steels with different surface finishes. Both bare and coated steel specimens were subjected to SOFC(IC)-relevant exposures and evaluated using complimentary surface analysis techniques.

Significant improvements were observed under simulated SOFC(IC) exposures with many coated specimens at  $\sim 800^\circ\text{C}$  relative to uncoated specimens: stable surface morphology; low area specific resistance (ASR  $<100\text{m}\Omega\cdot\text{cm}^2 > 1,000$  hours); and, dramatically reduced Cr volatility (>30-fold). Analyses and discussions of SOFC(IC) corrosion, advanced PVD processes and protective coating behavior are intended to advance understanding and accelerate the development of durable and commercially-viable SOFC systems.

## CHAPTER 1

## INTRODUCTION

Sustainable energy is an increasingly significant challenge for human society. Revolutionary innovations in renewable energy sources, conversion technologies and consumption efficiencies are required to ensure global socioeconomic and sociopolitical stability. In the portfolio of promising candidates for future energy conversion are solid oxide fuel cell (SOFC) systems. High energy conversion efficiencies, fuel flexibility and decreased or mitigated environmentally-sensitive emissions make SOFC systems attractive for many electric power generation applications. At present, SOFC systems are being developed for stationary large-scale centralized and distributed power generation, primary and auxiliary power generation for transportation, and portable power generation for small electronics [1-4]. SOFC systems utilize a wide-variety of fuels ranging from hydrogen-rich gas streams from renewable sources (bio-derived fuels or hydrogen from water electrolysis via solar or wind power) to natural gas (methane), coal gasification products (syngas), and transportation/logistics fuels, such as ethanol, diesel and JP-8. The highly efficient electrochemical conversion of these fuels in SOFC systems results in usable electric and thermal energy. Large-scale SOFC systems can be complemented with gas turbine, thermoelectric or other energy conversion devices to further elevate system efficiency to ~70% [5]. Despite substantial market opportunities, wide-spread SOFC use continues to be hindered by materials durability and cost challenges. This

dissertation aims to further understanding of materials stability and facilitate development of inexpensive and durable SOFC systems.

### Dissertation Overview

This study focuses on inexpensive metallic interconnects for SOFC systems and protective coatings (deposited by advanced physical vapor deposition techniques) to inhibit corrosion. The dissertation is organized into five chapters, the subjects of which are outlined in the Table of Contents. The first two chapters describe SOFC technology development, interconnect component degradation, theoretical considerations, and conventional protective coatings. The third chapter summarizes the technological resources employed for the study and outlines experimental details. The fourth chapter presents selected, representative study results and provides an interpretation of their significance. The fifth and final chapter summarizes study results and interpretations, and identifies future work needed in this area.

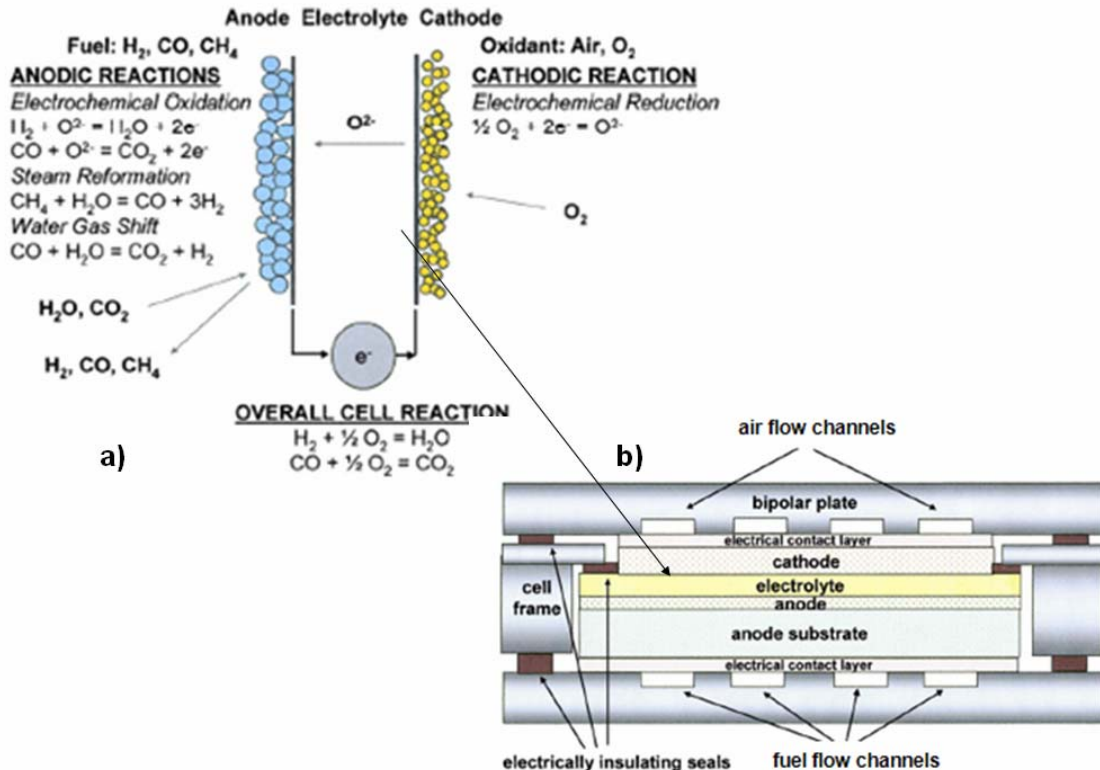
### Solid Oxide Fuel Cell (SOFC) Technology

Increasing demand for clean stationary, transportation and portable power has motivated significant investment in SOFC technology development globally [6]. SOFC development focuses on increasing system efficiency and durability, while reducing materials and processing costs. The United States Department of Energy's Solid-State Energy Conversion Alliance (SECA) program projects that a ~\$400/kW (electric power generation capacity) SOFC system capital cost would permit significant market

penetration into stationary power applications, and anticipates achievement of this goal by 2010 [7]. Recent advancements in SOFC materials and manufacturing show promising progress, however, system durability and cost challenges continue to impede commercialization.

A typical planar SOFC design and operation are shown schematically in Figure 1.1 [8]. Oxidant gas (typically oxygen in air) is fed to the porous ceramic oxide cathode, where it adsorbs, dissociates and is electrochemically reduced at the triple phase boundary (TPB) of the gas/cathode/electrolyte interface forming oxygen anions ( $O^{2-}$ ), which inject into unoccupied, or vacant oxygen anion lattice sites in the dense ceramic oxide electrolyte. Oxygen anions transport through the electrolyte (via solid state defects

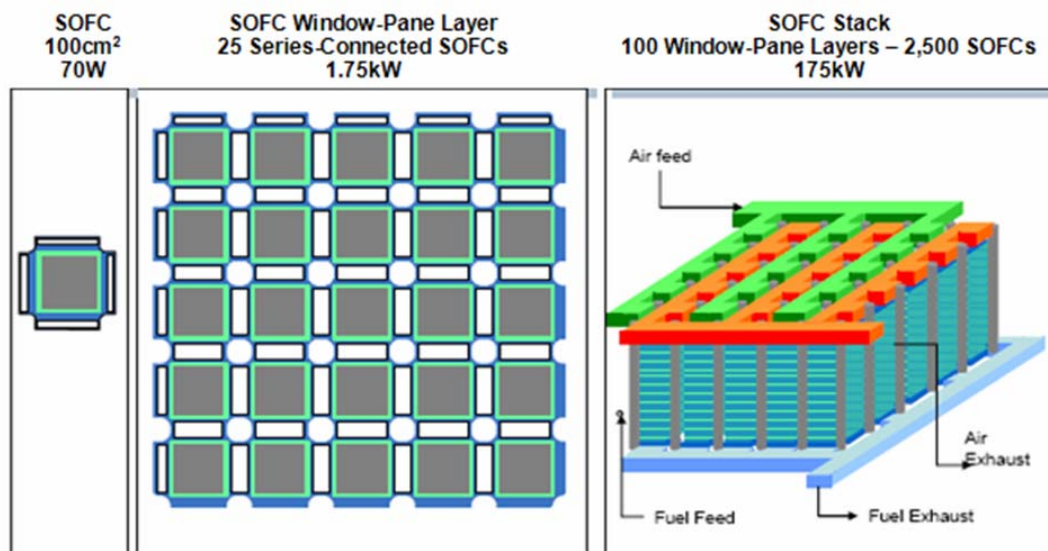
Figure 1.1. SOFC schematics: a) with associated reactions; b) planar repeat unit design [8].



– bulk and grain boundary oxygen vacancies) and electrochemically oxidize fuel(s) at the respective anode TPB (anode is typically a two-phase cermet: porous ceramic oxide mixed with metal). This produces oxide gas products of the fuel(s), e.g., H<sub>2</sub>O, CO, CO<sub>2</sub> and liberates electrons, which transport through the anode to the current-collecting bipolar plate (interconnect). Electrons continue through the interconnect to the adjoining (series-connected) cathode where they electrochemically reduce oxygen.

Driven by the oxygen concentration gradient across the electrolyte, the typical open-cell electrochemical potential (voltage) at each cell is ~1V, which reduces to ~0.7V at operational current densities of ~1A/cm<sup>2</sup>. To realize significant voltage, electrical series interconnection of cells into stack modules is required. Stack modules can then be connected for scalable power generation; an example design is shown in Figure 1.2 [4]. In this design, 25 planar SOFCs (~100cm<sup>2</sup>/SOFC \* 1A/cm<sup>2</sup> \* 0.7V ≈ 70W/SOFC) are interconnected in a 5x5 cell window-pane layer configuration, capable of ~1.75kW

Figure 1.2. Example of 5x5 cell “window pane-style” SOFC stack 175kW scale-up design [4].



electric power production. In an SOFC stack module comprised of 100 5x5 window-pane layers, ~175kW of electric power is possible, along with high-temperature (partially unconverted) fuel and air exhaust streams. Details on SOFC operation, integration with other energy conversion systems and comparison to other fuel cell types are found elsewhere [1-4].

### Historical Perspectives

In 1839, Sir William Grove developed the first documented fuel cell, which he termed the ‘gas voltaic battery’; a series, or battery of five cells consisting of dilute sulfuric acid electrolyte separating tubes charged with hydrogen and oxygen [9,10]. Since that time, a wide-variety of fuel cells have been developed, with five primary electrolyte types: polymeric; alkaline; acidic; molten carbonate; and, solid oxide. Each type has a unique range of optimal operating environments, with associated advantages and shortcomings [3,4]. Solid oxide fuel cell electrolytes require relatively high operating temperatures for sufficient ionic conductivity, which has related advantages and disadvantages compared with other fuel cell types. Advantages include:

- optional internal reforming or direct electrochemical oxidation of hydrocarbon fuels;
- the use of inexpensive electrocatalytic electrode materials, e.g., Ni cermet anodes and Mn-based ceramic oxide cathodes; and,
- usable high-temperature (and partially unconverted) exhaust streams.

Disadvantages owing to the high operating temperatures are predominately degradation-related, resulting from thermal-chemical (interdiffusion and/or corrosion) and thermal-

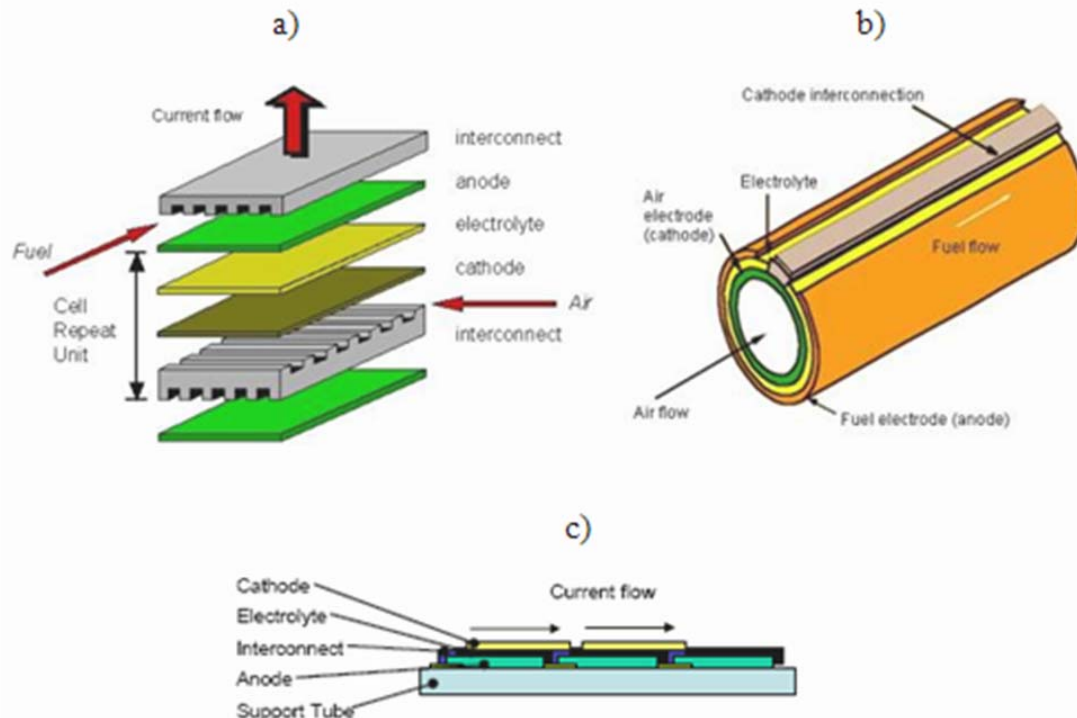
mechanical incompatibilities of SOFC component materials in complex operating environments.

The first documented commercial application of solid electrochemical materials began with German scientist and Nobel laureate, Hermann Walther Nernst, who in 1897 was awarded a patent for an electric lighting device known as the Nernst Lamp. Employing a zirconia ( $\text{ZrO}_2$ )-based electrode, the Nernst Lamp glowed via electric current (after first being externally heated to  $\sim 2000^\circ\text{C}$ ) [10]. In the 1930's, Swiss scientist Emil Baur and colleagues experimented with solid electrolytes composed of zirconium, yttrium, cerium, lanthanum, and tungsten oxides. These materials were found to exhibit low ionic conductivities, and were observed to adversely react with other solid materials and various gases, including carbon monoxide [9]. In the 1940's Ukrainian scientist, Prof. Oganes Davtijan investigated mixtures of oxide and carbide electrolyte materials, but met with similar challenges. Prof. Davtijan is also credited with the first published text on the subject (1947), with the translated title, "Problems of Direct Transformation of Chemical Energy of Fuel Into Electricity" [11]. By the late 1950's, research into solid fuel cell electrolytes had spread to several laboratories world-wide, but not even moderate success was achieved until the mid 1960's by Westinghouse, using zirconia-based electrolyte materials [1]. Ever-increasing energy-related concerns since that time now find numerous private entities, universities and national laboratories focusing on SOFC development.

### Recent Development

Since the 1960's many SOFC designs have been proposed, fabricated and demonstrated. Beginning with yittria ( $\text{Y}_2\text{O}_3$ )-stabilized zirconia (YSZ) solid electrolytes and noble metal electrodes, electrolyte-supported SOFC technologies were developed in the 1960-70's. In the 1980-90's, cermet (Ni/YSZ) anodes and oxide ceramic cathodes ( $\text{LaMnO}_3$  and  $\text{LaCoO}_3$ -based) and interconnects ( $\text{LaCrO}_3$ -based) were successfully demonstrated using both relatively thick (electrolyte-supported) and relatively thin (electrode-supported) YSZ electrolytes in planar, sealless tubular and segmented-in-series SOFC designs (Figure 1.3). To deliver adequate ionic conductivity, operating temperatures ranged from 800-1000°C, depending upon the YSZ electrolyte thickness, with thicker YSZ electrolytes requiring higher temperatures. Many tubular designs have

Figure 1.3. Examples of: a) planar; b) sealless tubular; and, c) segmented-in-series SOFC designs.



been operated for thousands of hours, and are technologically most advanced [1]. Interest in higher power densities and lower system cost, however, has recently directed attention toward intermediate temperature (600-800°C) planar SOFC designs, which may permit the use of significantly less expensive metallic interconnects (Figures 1.1, 1.3a).

### Planar SOFC(IC) Development

The planar SOFC(IC) is critical to successfully satisfy stack capital cost, operation and longevity criteria. In operation, the planar SOFC(IC) realizes simultaneous dual atmosphere (wet reducing and oxidizing) exposure at temperatures up to ~800°C. The SOFC(IC) physically and electrically connects the anodes and cathodes in adjacent cells, and seals to the electrolyte in these cells (see Figures 1.1, 1.3). The IC/electrode and IC/seal interfaces must exhibit chemical, mechanical and electrical stability throughout the desired >40,000 hour (~4.5 year) SOFC device lifetime, and through several hundred thermal cycles (from ambient to operating temperature) [12]. High-temperature metallic alloys have been considered for intermediate temperature (600-800°C) planar SOFC(IC)s due to improved mechanical properties and costs compared to ceramic alternatives, e.g., LaCrO<sub>3</sub>, but corrode in operating environments and degrade SOFC system performance. Development of planar SOFC(IC)s is described elsewhere in more detail [1-4,13].

### Functional Requirements

SOFC(IC)s must satisfy the following criteria and requirements:

- hermetic – must be impervious to fuel and oxidant gases to prevent catastrophic leakage;
- thermal-mechanically stable – must have thermal expansion coefficient (CTE) comparable with adjoining SOFC components to avoid excessive thermal-mechanical stresses leading to brittle fracture (especially during thermal cycle events – ambient temperatures to 800°C);
- thermal-chemically stable - must be compatible with adjoining SOFC components and gases so as to not form deleterious reaction products while maintaining chemical, morphological and dimensional stability in both reducing and oxidizing environments; and,
- electrically stable – must maintain low area specific resistance (ASR)  $<100\text{m}\Omega\cdot\text{cm}^2$ , which translates to a voltage drop of  $<100\text{mV}$  (or  $\sim 10\%$  of the  $\sim 1\text{V}$  open circuit cell potential) across the SOFC(IC) considering a  $100\text{cm}^2$  active area and  $1\text{A}/\text{cm}^2$  current density.

Combined satisfaction of the above requirements must be achieved to the extent that SOFC stack voltage degradation is less than 0.1% per 1,000 hours throughout the desired 40,000 hour ( $\sim 4.5$  year) device lifetime [12]. In addition, SOFC(IC) materials must also be amenable to high-throughput (and low cost) production to meet anticipated market demands, e.g., 700MW/year planar SOFC module production at  $\sim 70\text{W/SOFC}$  would require the production of  $\sim 10,000,000$  interconnect components annually.

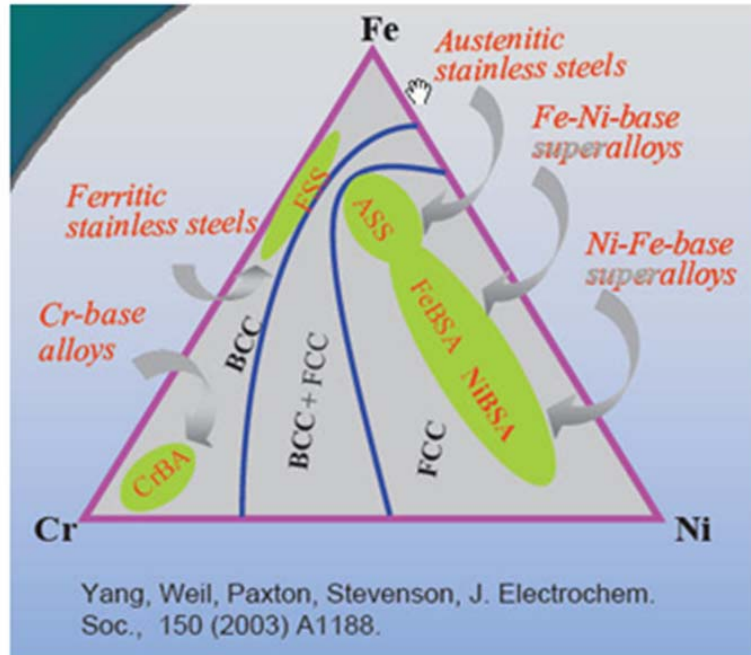
### Ceramic Materials

To meet the demanding requirements for higher temperature (~800-1,000°C) SOFC(IC)s, various ceramic oxide materials have been widely used. LaCrO<sub>3</sub> is a well-characterized perovskite (ABO<sub>3</sub>) refractory oxide that has been used since the 1970's as an SOFC(IC) material. LaCrO<sub>3</sub> exhibits adequate interconnect performance, but is most often tailored via dopants, e.g., Ca, Sr, Co, to enhance SOFC(IC)-related properties [1]. Extensive optimization work has been performed on fabrication techniques and defect chemistry of LaCrO<sub>3</sub>-based interconnects [1]. Unfortunately, high cost, instabilities (especially in fuel/anode atmospheres) and fabrication challenges continue to be limiting [1-4, 13]. LaCrO<sub>3</sub>-based coating materials for metallic SOFC(IC)s have also been investigated [18-20, 63,64].

### Metallic Alloys

At lower operating temperatures ( $\leq 800^{\circ}\text{C}$ ), heat resistant, high Cr and/or Ni-based alloys are attractive interconnect materials. Figure 1.4 shows an Fe/Ni/Cr ternary phase diagram at 800°C [14]. The three regions shown in this diagram indicate predominance of face or body centered cubic (FCC or BCC) lattice structures and highlight some alloy compositions of technological significance to other applications. High Cr-content, Fe-based alloys (BCC-ferritic stainless steels) are preferred for SOFC(IC)s due to their relatively low-cost, coefficient of thermal expansion (CTE) match with conventional SOFC ceramic electrolyte and electrode components, and the formation of an electrically conductive Cr<sub>2</sub>O<sub>3</sub>-based thermally grown oxide (TGO) surface scale in SOFC(IC) operating environments [14].

Figure 1.4. Fe/Cr/Ni ternary phase diagram [14].



Unfortunately, continued TGO scale growth introduces deleterious electrical, chemical and mechanical incompatibilities with adjoining SOFC components, degrading their performance and leading to system failure.

An extensive investigation of several high-temperature alloys revealed that for improved oxidation resistance and electrical conductivity, either new alloys must be developed, or surface engineering of existing alloys is required [14]. Among those in the former category is Crofer 22 APU (Crofer), a specially-designed ferritic stainless steel (Cr 20-24%), with reduced Si content and engineered additions of Mn, Ti and La (available through ThyssenKrupp VDM) [15]. Crofer is characterized by the formation of an electrically conductive Cr-Mn TGO scale layer during SOFC cathode gas phase (air) exposure, exhibiting low ASR and other SOFC(IC) relevant virtues [65-67]. During

extended 800°C SOFC(IC) exposures using Crofer, however, continued TGO scale growth (dominated by an underlying Cr<sub>2</sub>O<sub>3</sub> layer) increases ASR and results in other undesired effects [16,17]. To enhance SOFC(IC) durability of both specially-designed and commercially-available alloys, surface engineering via protective coatings is ongoing in laboratories world-wide, and is the topic of this investigation.

#### Investigation Purpose, Significance and Limitations

The overall objectives of this work are to:

- further understanding of planar SOFC(IC) corrosion;
- develop protective coating technology and materials to inhibit corrosion; and,
- facilitate rapid development of inexpensive SOFC systems.

Limitations to this investigation lie in the complexities of experimentally simulating SOFC interconnect operating environments and interpreting data in the context of laboratory-scale vs. industrial/commercial-scale settings. To overcome these limitations, consistent experimental protocols are being adopted among SOFC researchers, and collaboration among public and private SOFC developers is accelerating.

#### Definition Of Terms

SOFC – Solid Oxide Fuel Cell

SOFC(IC) SOFC Interconnect

SEM – Scanning Electron Microscope

TEM – Tunneling Electron Microscope

EDS – Energy Dispersive X-Ray Spectroscopy

EBSD – Electron Backscattered Diffraction

SAED – Selected Area Electron Diffraction

XRD – X-Ray Diffraction

GI-XRD – Grazing angle Incidence X-Ray Diffraction

RBS – Rutherford Backscattering Spectroscopy

PVD – Physical Vapor Deposition

CVD – Chemical Vapor Deposition

LAFAD – Large Area Filtered Arc Deposition

EBPVD – Electron Beam Physical Vapor Deposition

FAPSID – Filtered Arc Plasma Source Ion Deposition

FA-EBPVD – Filtered Arc-assisted Electron Beam Physical Vapor Deposition

$\Delta G$  – Gibbs Free Energy Change

R – Universal Gas Constant

T – Absolute Temperature

CTE – Coefficient of Thermal Expansion

TGO – Thermally Grown Oxide

## CHAPTER 2

## SOFC METALLIC INTERCONNECT DEGRADATION

Significantly lower cost compared with ceramic counterparts has directed attention toward commercially-available and specially-designed corrosion-resistant high-temperature metallic alloys for SOFC(IC)s operating  $\leq 850^{\circ}\text{C}$  [1-4]. These alloys can be categorized by two primary types: chromia ( $\text{Cr}_2\text{O}_3$ ) formers; and, alumina ( $\text{Al}_2\text{O}_3$ ) formers. Selective surface oxidation of Cr or Al in the alloys, and the refractory properties of their respective TGO surface scales ( $\text{Cr}_2\text{O}_3$  or  $\text{Al}_2\text{O}_3$ ) protect the bulk alloy from environmental attack. Alumina-based TGO scales are known to grow slower and provide more protection than chromia-based TGO scales; however, alumina formers are not favored for SOFC(IC)s due to alumina's poor electronic conductivity. Some chromia-forming alloys are promising candidates for SOFC(IC)s, however continued TGO scale growth and associated deleterious effects are limiting. Through bulk alloy development, TGO scale modifications to enhance SOFC(IC) performance of chromia formers has met with some success; however, corrosion continues to present challenges [13]. Understanding SOFC(IC) corrosion provides insight into protection via functional coating technology and materials development.

Metal Alloy Corrosion at High-temperatures

High-temperature corrosion of metals and metal alloys has been the subject of numerous texts and peer-review periodicals, e.g., Diffusion in Solids and High-

temperature Oxidation of Metals [21], Introduction to the High-Temperature Oxidation of Metals [22], Handbook of Corrosion [32], and High-Temperature Oxidation of Metals [68], to name a few. Several mechanistic corrosion models have been proposed and experimentally verified for extensively investigated pure materials (metals). Modeling high-temperature corrosion of multi-component SOFC(IC) alloys in dynamic gas environments while contacting other solid materials is significantly more complex. Careful experimentation coupled with system thermodynamics, defect chemistry and kinetics analyses facilitates understanding of corrosion mechanisms. In turn, this understanding guides corrosion-resistant materials development. For the SOFC(IC) application, both alloy development and surface engineering are aimed at enhancing corrosion-resistance to enable inexpensive materials.

### Thermodynamics

Understanding high-temperature SOFC(IC) corrosion behavior requires determination of whether a particular component within the alloy will react with contacting gas and/or solid-state components (e.g., oxygen in air, contacting cathode and seal materials). Equilibrium thermodynamics is a critical tool in this assessment [22, 68].

For the chemical reaction,



the Gibbs free energy of reaction at equilibrium, is given by,

$$\Delta G^\circ = -RT \ln K_{eq} \quad (2.2)$$

where  $K_{eq}$  is the reaction equilibrium constant defined as,

$$K_{eq} = \frac{a_C^c a_D^d}{a_A^a a_B^b} \quad (2.3)$$

in which  $a_i$  denotes activity of species  $i$ . Activity defines a material's deviation from its standard state. Activity is a dimensionless number and is often represented at high-temperatures by

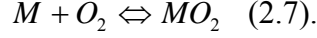
$$a_i = \frac{p_i}{p_i^\circ} \quad (2.4)$$

where  $p_i$  is the vapor pressure over a condensed species, or the partial pressure of a gaseous species, and  $p_i^\circ$  is the same quantity corresponding to the standard state (usually 25°C and 1atm). A related quantity, the chemical potential,  $\mu_i$ , is related to activity by,

$$\mu_i = RT \ln(a_i) + \mu_i^\circ \quad (2.6)$$

where  $\mu_i^\circ$  is the chemical potential of species  $i$  at standard state.

Consider the oxidation of a tetravalent metal, M, with gaseous oxygen;



The equilibrium constant for this reaction is:

$$K_{eq} = \frac{a_{MO_2}}{a_M a_{O_2}} \quad (2.8).$$

Assuming equivalent (unit) activities of both solid species (M and MO<sub>2</sub>) for pure metals and metal oxides, rearranging (2.2) yields the equilibrium partial pressure of oxygen at which the metal and its oxide coexist (the dissociation pressure of the oxide) [22]:

$$p_{O_2}^{M / MO_2} = \exp\left(\frac{\Delta G^\circ}{RT}\right) \quad (2.9).$$

The metal oxide formation free energy,  $\Delta G^\circ$ , and heat capacities are well-known for many species, and are useful for comparing the relative stabilities of metals within given temperature and/or oxidizing conditions. Graphical interpretation for this comparison is afforded by Ellingham diagrams, which are also used for metal interactions with nitrogen and carbon. Ellingham diagrams typically plot Gibbs free energy of the oxidation reaction versus temperature with separate scales relating to the equilibrium partial pressures for oxidation or reduction of metal or metal oxide species, respectively [22].

When considering metal oxidation equilibria for alloys, metal and metal oxide activities must be taken into account since they are no longer unity;

$$p_{O_2}^{M/MO_2} = \frac{a_{MO_2}}{a_M} \exp\left(\frac{\Delta G^\circ}{RT}\right) \quad (2.10).$$

Alloy design often exploits differences in activities and oxide formation free energies of constituent metals to form protective (oxidation-barrier) TGO surface layers. Knowledge of species' activities, their thermochemical properties and their coupled interactions facilitates assessment of thermodynamically-favored corrosion-product compositions. The complex corrosive SOFC(IC) environments and demanding functional requirements challenge alloy design and TGO scale engineering.

Thermodynamics also finds utility in understanding defect chemistry of ionic solids (metal oxides). Defect chemistry helps to explain transport phenomena in TGO scales, which ultimately governs their evolution and characteristics. In stoichiometric crystalline materials, two types of defects are common; these are Schottky and Frenkel defects. Schottky defects are comprised of an equal number (pair) of cations and anions, which are absent from their otherwise occupied crystalline lattice positions and create

associated cation and anion vacancies. Frenkel defects are also pairs comprised of interstitial ions (typically cations) and resultant cation vacancies in the lattice. These solid state defects help explain ionic transport through ceramic TGOs, but do not explain simultaneous electron transport, which is observed in high-temperature metal corrosion processes [21,22,68]. For simultaneous ion and electron transport in solid materials, significant presence of defects (crystal impurities (dopants) and/or non-stoichiometry) is assumed. To describe point defect chemistry in crystals, Kröger-Vink notation is commonly used (Table 2.1) [24]. Other defects, such as surfaces or grain boundaries between crystals often serve as point defect sinks.

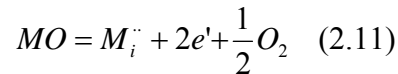
Table 2.1. Kröger-Vink notation for point defects in crystals.

Divalent ions as in  $\text{MX} = \text{M}^{+2}\text{X}^{-2}$  compound are considered; superscript dots (•) indicate positive excess charge, dashes (◦) indicate negative excess charge, and x (x) indicates no excess charge with respect to the neutral, unperturbed lattice.

Notation	Point Defect
$V_M^{\bullet}$	Vacant M site
$V_X^{\circ}$	Vacant X site
$M_M^x$	Metal ion on lattice site
$X_X^x$	X ion on lattice site
$L_M^{\circ}$	$\text{L}^+$ dopant ion on $\text{M}^{+2}$ lattice site
$N_M^{\circ}$	$\text{N}^{+3}$ dopant ion on $\text{M}^{+2}$ lattice site
$e^{\bullet}$	Free electron
$h^{\circ}$	Free (electron) hole
$M_i^{\circ}$	Interstitial M ion
$X_i^{\bullet}$	Interstitial X ion

An example point defect (metal excess) analysis in a non-stoichiometric metal oxide is developed below, with a summary of other common non-stoichiometric metal oxide defects following.

Consider metal excess defect formation in a metal oxide with divalent metal, described by



where  $M_i^{\cdot\cdot}$  is an interstitial metal ion with effective double positive charge, which is balanced by two free (conduction band) electrons. This results in metal oxide non-stoichiometry and n-type electronic conductivity. Assuming the defects are dilute (obeying Henry's law - concentration directly proportional to activity), with  $a_{MO} \approx 1$ , and activities being directly proportional to concentrations or partial pressures, application of Equation 2.3 yields,

$$K_{eq} = C_{M_i^{\cdot\cdot}} C_{e'}^2 p_{O_2}^{1/2} \quad (2.12)$$

where  $C_{M_i^{\cdot\cdot}}$ ,  $C_{e'}$  are the respective concentrations of interstitial metal ions and conduction band electrons, and  $p_{O_2}$  is the partial pressure of oxygen. Noting that  $2C_{M_i^{\cdot\cdot}} = C_{e'}$  and constant  $K_{eq}$ , rearrangement of Equation 2.12 yields the equilibrium conduction band electron concentration dependence on oxygen partial pressure:

$$C_{e'} \propto p_{O_2}^{-1/6} \quad (2.13).$$

The same general treatment can be applied to other defects: non-metal or oxygen deficits; impurities/dopants; cation heterovalence; or, electronic defects [21,22,68].

Conductivity experiments in varying oxygen partial pressures thus yields critical information on defect chemistry and transport mechanisms to help explain high-temperature conductivity in ceramic oxides.

Another important consideration is the temperature dependence of defect concentration, which when considered dilute is approximated by:

$$x \propto A \exp\left(\frac{-E_d}{RT}\right) \quad (2.14)$$

where  $x$  is the defect concentration,  $A$  is a pre-exponential factor (having units of concentration) and  $E_d$  is the activation energy for defect formation. With this approximation, and estimating 50KJ/mol defect formation activation energy, the fractional increase in defect concentration ( $x$ ) from 300K to 1000K would be  $\sim 10^6$ . Exponential temperature dependence of defect concentration also helps explain high-temperature conductivity in ceramic oxides.

Combining the two effects (temperature and oxygen partial pressure) guides defect equilibria calculations in non-stoichiometric oxides, and permits assessment of defect chemistry's role in high-temperature metal surface corrosion.

### Kinetics

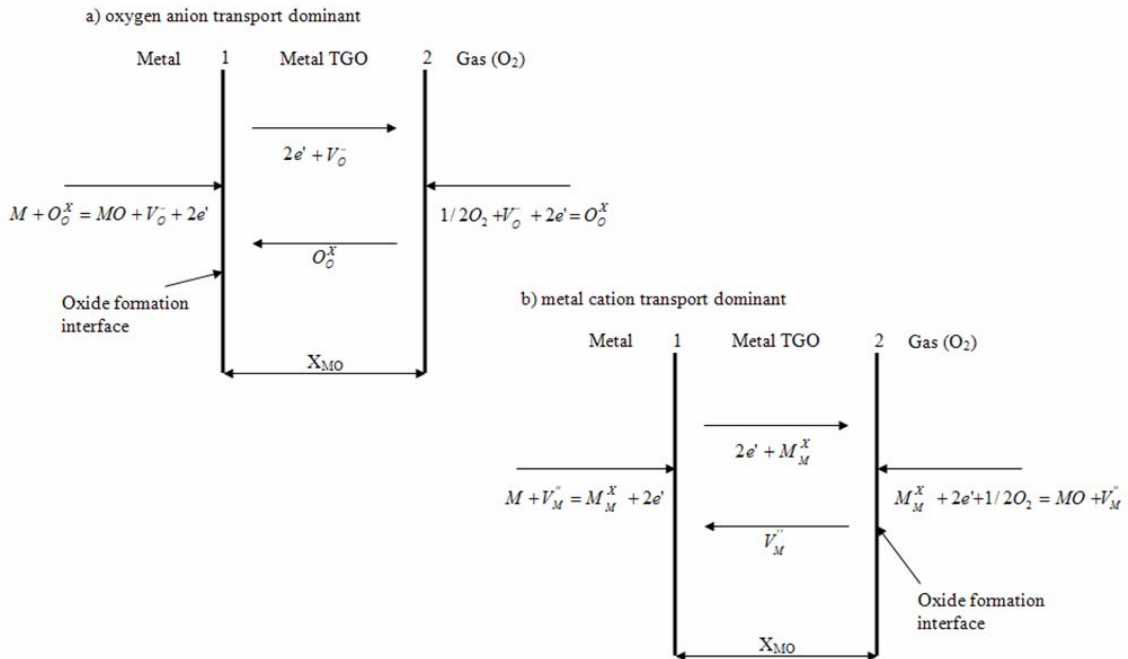
Although thermodynamic equilibrium provides the energetic driving-force for corrosion, kinetic processes often dictate TGO scale formation and growth characteristics. High-temperature corrosion of metals proceeds by several processes. In the initial oxidation of a clean metal surface, molecular oxygen adsorbs onto the metal surface, where it then dissociates and dissolves into and/or reacts (via several potential

mechanisms) with the metal to form metal oxide nuclei. The adsorption and initial oxide formation are functions of the metal surface (crystallographic orientation, defects and preparation) and impurities in both the metal and gas [68]. As the metal oxide nuclei grow and spread from nucleation sites, a continuous thin metal TGO layer forms over the entire metal surface. The subsequent metal TGO layer thickening is substantially determined via transport of oxidizing species (metal or oxygen ions) through the layer. At high-temperatures, the initial surface adsorption and metal oxide formation reaction(s) proceed very rapidly compared with the subsequent rate of transport of species through the TGO layer [21,22,68]. The former is typically determined by reaction rate-limiting processes, and exhibit either linear or logarithmic time-dependences; the latter is predominately diffusion-controlled, and usually exhibits a parabolic time-dependence of TGO thickness. TGO scale formation and growth may involve sequential processes with varying time-dependencies, and is often difficult to model. Developments of linear and logarithmic rates are provided elsewhere [22,68], with a simplified development of parabolic rate time-dependence following.

Figure 2.1 schematically illustrates the reaction and transport processes occurring in the second stage of surface oxidation at high-temperature. Assuming rapid reaction rates at high-temperatures (i.e., thermodynamic equilibrium is established at both metal/oxide and oxide/gas interfaces), metal oxide growth is typically dominated by either the inward transport of oxygen anions toward the metal (Figure 2.1a), or the outward transport of metal cations (Figure 2.1b). As both species are ionic, simultaneous transport of electrons is requisite to ionize the metal or adsorbed oxygen, thus requiring

non-stoichiometry or other defects in the metal oxide. Transport mechanisms for either ionic species include: lattice (bulk) transport via ion vacancies or interstitial sites within grains; and, grain boundary transport.

Figure 2.1. Schematic illustration of high temperature metal oxidation reactions and transport processes for two scenarios: a) oxygen anion transport dominant; and b) metal cation transport dominant



Transport mechanisms for other charge carriers (electrons or holes) include: conduction band transport; or, polaron transport (a polaron is a quasi-particle consisting of a combined charge carrier (electron or hole) and strain energy of localized elastic lattice deformation [e.g., vacancy], which transport together [23]).

It is generally considered that the mobility of ions are orders of magnitude less than that of electrons or electronic defects, and therefore primary focus is placed on ionic transport [21,22,68]. Considering outward cation flux as the controlling TGO scale growth mechanism (Figure 2.1b), a simplified formulation to describe TGO scale parabolic growth rates follows. First, the flux of cations, is assumed equal and opposite to cation vacancies, as in

$$j_{M^+} = -j_{V_M^+} = D_{V_M^+} \frac{C_{V_M^+}^2 - C_{V_M^+}^1}{X_{MO}} \quad (2.15)$$

where  $D_{V_M^+}$  is the effective diffusion coefficient for metal ion vacancies through the metal oxide film,  $C_{V_M^+}^2 - C_{V_M^+}^1$  is the difference in metal ion vacancy concentrations (at interface 2 and 1, respectively – see Figure 2.1), and  $X_{MO}$  is the thickness of the metal oxide. In terms of metal oxide scale thickening, Equation 2.15 can be used to provide the differential parabolic rate law,

$$j_{M^+} = \frac{1}{V_{MO}} \frac{dX_{MO}}{dt} \quad (2.16)$$

where  $V_{MO}$  is the specific molar volume of the metal oxide, and  $\frac{dX_{MO}}{dt}$  is the rate of metal oxide thickening. Assuming equilibrium at both interface 1 and 2 (cation vacancy concentrations at these locations are constant) and constant diffusivity through the metal oxide, integration of Equation 2.16 (assuming  $X_{MO} \approx 0$  @  $t = 0$ ) yields the common integrated parabolic rate law:

$$X_{MO}^2 = 2k't \quad (2.17).$$

The parabolic rate constant,  $k'$ , encompasses the metal oxide molar volume, the driving-force for ionic transport (cation vacancy concentration gradient across the TGO scale) and the resistance to transport (diffusion coefficient) within the metal oxide film. Values of  $k'$  are given in different units depending upon the methods used for determination, e.g.,  $\text{cm}^2/\text{s}$  for oxide thickening [22].

Many formalisms to accurately describe high-temperature corrosion phenomena in specific environments have been developed; perhaps the most fundamental of which is Wagner's theory of oxidation [25]. The development of this theory is described in detail elsewhere [22,25,68], with some important features summarized here. Using Wagner's theory, the parabolic rate laws (Equations. 2.16, 2.17) are concluded; however, further considerations are made for electric potential gradients and non-constant ionic conductivities (diffusivities) across the TGO scale thickness. Parabolic rate constants are often determined from integrals of diffusion coefficients, which are dependent on local thermodynamic conditions throughout the TGO scale. An example in which metal cation transport is the limiting transport mechanism for scale growth is,

$$k' = \frac{1}{RT} \int_{\mu_M^2}^{\mu_M^1} D_M d\mu_M \quad (2.18),$$

where  $D_M$  is the metal ion diffusion coefficient, which is assumed a function of the metal species' chemical potential,  $\mu_M$  [22]. Often, parabolic rate constants are more easily measured directly than are diffusion coefficients, which can be subsequently elucidated via combining rate measurements with defect equilibria considerations. For pure metals,

these analyses are in excellent agreement with experiment. Similar analyses can be applied to understand SOFC(IC) corrosion behavior with and without protective coatings.

### Degradation Mechanisms

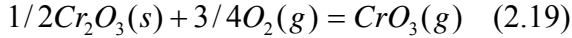
As TGO scales continue to grow on SOFC(IC) metal alloy surfaces, protection limitations arise. These include scale spallation (debonding), break-away oxidation, increased electronic (area specific) resistance, and deleterious material interactions. A brief summary of degradation mechanisms follows, leading into a discussion of SOFC(IC) protective coatings.

TGO scale spallation occurs when stress energy stored within the growing TGO layer exceeds that of the interfacial strength between the TGO and underlying metal, causing the TGO to buckle or debond (spall) from the metal surface [26, 27]. The energy release rate responsible for the spallation may depend on both metal and TGO scale characteristics, including chemical and phase compositions, surface roughness and exposure conditions, e.g., local corrosion environment or thermal cycling [26,27]. TGO scale spallation exposes underlying metal to continued environmental attack, and introduces spalled TGO scale material into the service environment. In the SOFC(IC) application, this may inhibit gas transport in small electrode chamber gas channels.

Increased electronic area specific resistance (ASR) results from TGO scale growth. As the TGO scale thickness increases, so does the electron (or electron defect) transport path length. Assuming constant electronic conductivity within the scale, ASR increase is directly proportional to scale thickening, and therefore commonly exhibits a parabolic time dependence. In many cases, TGO scale composition evolves during

exposure, thus changing the effective electronic conductivity and ASR. For example, in many ferritic steel (Fe/Cr) alloys with Mn as a minor alloy element, the TGO scale evolves a layered stratigraphy, with slow-forming  $\text{CrMn}_2\text{O}_4$  (spinel)-based layer at the gas interface and a  $\text{Cr}_2\text{O}_3$  (corundum)-based layer at the metal interface, which may be explained by the high oxygen affinity of Mn compared to Cr or Fe. Subsequent to  $\text{CrMn}_2\text{O}_4$  surface layer formation, continued TGO growth is dominated by the underlying  $\text{Cr}_2\text{O}_3$ . The electronic conductivity of  $\text{CrMn}_2\text{O}_4$  is an order of magnitude larger than that of  $\text{Cr}_2\text{O}_3$ , and observed slowing decreasing ASR, followed by its parabolic growth has been attributed to the evolving TGO scale stratigraphy [16,29]. In application, the SOFC(IC) (or TGO scale) must remain in intimate electrical contact with the adjoining cathode material, which facilitates electron transport through the SOFC stack. The total interconnect/cathode ASR is thus a measure of the TGO scale resistivity and contact resistances at the TGO/cathode and TGO/alloy interfaces [31]. Continued TGO scale growth and chemical evolution may compromise these interfaces.

Another significant degradation mechanism results from TGO scale evaporation. Solid-phase  $\text{Cr}_2\text{O}_3$  reacts with air and water vapor to form volatile Cr(VI) species, e.g.,



and,



In the SOFC cathode environment, Cr volatility from metallic interconnects has been implicated in SOFC performance degradation [30,34-36]. Depending upon cathode and electrolyte materials, volatile Cr species have been reported to adsorb and perhaps

undergo solid-state and or electrochemical reaction (forming condensed phase Cr species) at the cathode/electrolyte TPB, as well as throughout the cathode [35]. Recent attention has also focused on direct surface transport of Cr species which may migrate from the TGO into the cathode and adversely effect performance [37]. Regardless of deleterious effects on SOFC performance, Cr volatility (and/or surface transport) effectively consumes the TGO scale, which can reach steady-state thicknesses between growth and evaporation under appropriate conditions [22,68]. This process results in metal surface recession which, depending upon chromia forming alloy component thickness, may impact mechanical integrity [28]. As suggested in Equations 2.19 and 2.20, Cr volatility depends on  $\text{Cr}_2\text{O}_3$  activity in the TGO scale or coating, which depends on composition of the Cr-containing oxide. Some Cr-containing oxides, such as  $(\text{Cr},\text{Mn})_3\text{O}_4$  exhibit lower Cr-volatilities than  $\text{Cr}_2\text{O}_3$  [16]. This is due not only to the lower Cr concentration within these species, but also greater lattice stability, which effectively lowers  $\text{Cr}_2\text{O}_3$  thermodynamic activity [36]. More discussions on this are presented in Chapter 4.

A phenomena termed, “break-away oxidation” occurs when the reservoir of the selectively oxidized and protective element (e.g., Cr/Al) in the high-temperature alloy becomes depleted, and its relatively low activity permits oxidation of other, more rapidly oxidized alloy elements, e.g., Fe [32]. This phenomena is especially pronounced in thin foil alloy specimens. To avoid this phenomena in this study, alloy specimen thicknesses of about 1mm were used, as noted in Chapter 3.

Overall, protective surface coatings may be required to achieve satisfactory long-term (40,000 hour) SOFC(IC) performance using commercially-available metal alloys at ~800°C.

#### Protective Coatings and Example Applications

High-temperature corrosion resistant coatings have been used for decades in applications ranging from power generating gas turbines to aircraft and automobile components. The objective is to create a physical and chemical barrier between the component (usually chosen for its bulk properties and cost) and corrosive service environments. Very high-temperature coatings (>1,000°C) are typically thick (>50µm) ceramic oxide coatings (e.g., doped ZrO<sub>2</sub>) which provide the often necessary temperature gradients between the alloy component and the service environment. The temperature gradient is achieved by phonon scattering and absorption mechanisms within the ceramic oxide coating; however, oxygen and other corrosive species continue to penetrate and degrade the underlying alloy component. In many cases, a layered coating approach is adopted. In this stratigraphy, so-called “bond-coatings” (often diffusion-coated metal-aluminides) are applied directly to the alloy before the thick (>50µm) ZrO<sub>2</sub> coating. During operation, a TGO scale is formed between the ceramic top coat and metallic bond coat, which promotes interlayer adhesion and provides a diffusion barrier against corrosive species’ penetration to the alloy component. Current state-of-the art, very high-temperature coating technologies are aimed at further increasing the possible service

temperature, while also securing erosion resistance, cyclic stability (fatigue life) and overall durability.

Compared with these very high-temperature applications, SOFC(IC) protective coatings take on different challenges. In addition to satisfying the demanding requirements specified in Chapter 1, SOFC(IC) surface engineering (coatings or surface treatments) must also not add prohibitive materials or processing costs.

### Conventional Protective Coating Deposition Techniques

Many different conventional coating deposition techniques have been investigated to deposit conductive polycrystalline ceramic coatings on alloys for SOFC(ICs). These coatings include: typical perovskite cathode materials, such as LSM ( $\text{La}_x\text{Sr}_{1-x}\text{MnO}_3$ ); previous interconnect materials (doped lanthanum chromites  $\text{LaCrO}_3$ ); and conductive oxide spinels, such as  $(\text{Cr},\text{Mn})_3\text{O}_4$  and  $(\text{Co},\text{Mn})_3\text{O}_4$  [18-20,38-51,63,64]. The polycrystalline ceramic oxide coating materials are typically prepared via conventional precipitation or pyrolysis from solution, followed by calcination, sintering and milling processes. The resultant powders can then be applied directly as coatings via thermal spray techniques, or prepared as solutions in aqueous mediums using binding and dispersion-agents. Solution-based coating deposition techniques include screen-printing, sol-gel, slurry (dip coating), electrolytic, and others [52]. These coatings have met with varying degrees of success; however, long-term stability remains challenging due to the dynamic SOFC(IC) service environment and continued transport of corrosive species leading to degradation. Improvements in composition and microstructure control have

advanced durability of conventional ceramic SOFC(IC) coatings, but many desirable coating features (density/barrier properties) favor the use of vapor deposition approaches, as described in Chapter 3.

## CHAPTER 3

ADVANCED COATING TECHNOLOGY  
FOR SOFC(IC) PROTECTIONOverview

Vapor deposition technology includes both chemical and physical vapor deposition (CVD and PVD, respectively). CVD involves a gas-phase reaction, which deposits the products of the reaction onto nearby surfaces. In the case of many CVD ceramic oxide coatings, vaporized metal-halide or metal-organics are decomposed in an oxidizing gas phase, condensing metal oxide product coatings onto substrate surfaces. Surface diffusion (e.g., pack cementation) CVD techniques have been explored to create surface layers saturated with rare-earth metals. This approach has been observed to enhance TGO scale characteristics (reduced growth rate, improved adhesion); however, long-term performance is compromised by continued TGO scale growth. These widely-used processes result in protective coatings for common components in many industries (die casting dies, bond coatings for turbine blades, etc.) However, poor control of coating characteristics (composition/microstructure/density) and disposal of associated hazardous process byproducts has directed attention to PVD processes for many applications, including the SOFC(IC).

Physical Vapor Deposition Technology

PVD techniques encompass sputtering and evaporation processes. These are used widely in semi-conductor fabrication applications, and also in high through-put

commercial applications, such as coatings for architectural glass and packaging materials. Common PVD techniques include magnetron sputtering, electron beam evaporation, thermal evaporation, pulsed laser ablation and vacuum arc evaporation. PVD processes create vapors of target material (sputtered or evaporated), which then transport in the gas (or plasma) phase to deposit on solid substrate surfaces. Often, reactive gases such as oxygen, nitrogen or methane are added to promote formation of oxide, nitride, carbide, or complex ceramic or cermet combinations. By controlling vapor deposition rates and reactive gas supplies, coatings with engineered compositions and stratigraphies are possible. Energies and rates of depositing (and reacting) species govern coating growth and properties, and are characteristic of the PVD technique. Detailed and comparative discussions of common PVD techniques are provided elsewhere [53,54].

Apart from those previously described, PVD coatings for high-temperature applications were historically developed for cutting and machining tool applications, in which resistance to both corrosion and wear was desirable. These coatings range from carbides and nitrides to oxides and their combinations, deposited by reactive magnetron sputtering, electron beam evaporation, or vacuum arc evaporation. PVD coating technology continues to enable longer life of numerous industrial components [53,54].

The two advanced PVD techniques discussed further below are the patented large area filtered vacuum arc vapor deposition (LAFAD), and hybrid filtered arc plasma-assisted electron beam evaporation (FA-EBPVD) [55,56]. These two deposition techniques have demonstrated promise in forming protective SOFC(IC) coatings. This work presents an initial evaluation of that promise, in addition to analyses of

experimentally observed behaviors and properties of the LAFAD and FA-EBPVD coatings in simulated SOFC(IC) exposures.

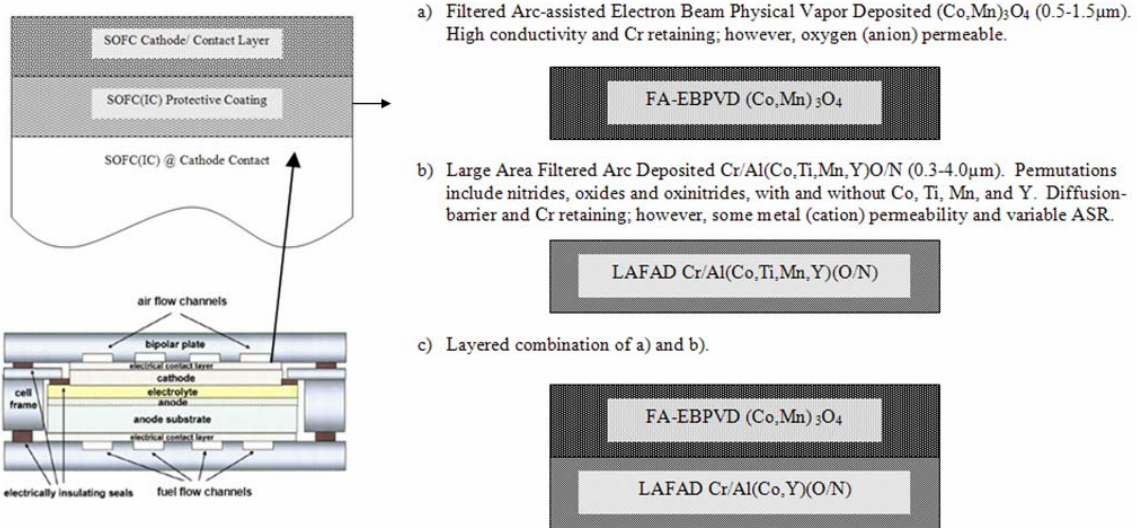
### SOFC(IC) Coating Structures

In addition to protecting against SOFC(IC) corrosion, the functional requirements specify that any coating must also maintain low ASR. This is challenging for many conventional electronically-insulating ceramic compositions, which are known to serve well as diffusion-barriers. SOFC(IC) coatings must exhibit a combination of high electronic conductivity ( $\text{ASR} < 100 \text{m}\Omega\cdot\text{cm}^2$ ) and sufficiently low ionic conductivity to prevent rapid TGO scale growth. For this, various conductive ceramic perovskite and spinel coating materials have been explored using conventional and vapor-based deposition techniques [17-20,29,38-51,63,64]. This investigation focused on two main coating material types:

- LAFAD Cr and Al-based nitrides, oxides and oxinitrides, with dopant elements including Co, Mn, Ti, and Y ( $\sim 0.3\text{-}4.0 \mu\text{m}$ ); and,
- FA-EBPVD  $(\text{Co,Mn})_3\text{O}_4$  spinel ( $0.5\text{-}1.5 \mu\text{m}$ ).

SOFC(IC) coating designs are shown schematically in Figure 3.1. Permutations in the basic design include both composite and layered structures, with varying layer compositions and thicknesses.

Figure 3.1. SOFC(IC) advanced PVD coating designs.



### Research Methods

High Cr, ferritic stainless steel coupons were used to simulate SOFC(IC) alloys, with Si wafers, and other alloy coupons included in the coating deposition processes to observe variations in coating composition, thickness, stress and adhesion. A wide-variety of coating deposition process parameter and substrate combinations were explored. Subsequent to coating deposition, coupon specimens were evaluated for SOFC(IC) relevant performance using a range of experimental procedures and surface analysis techniques.

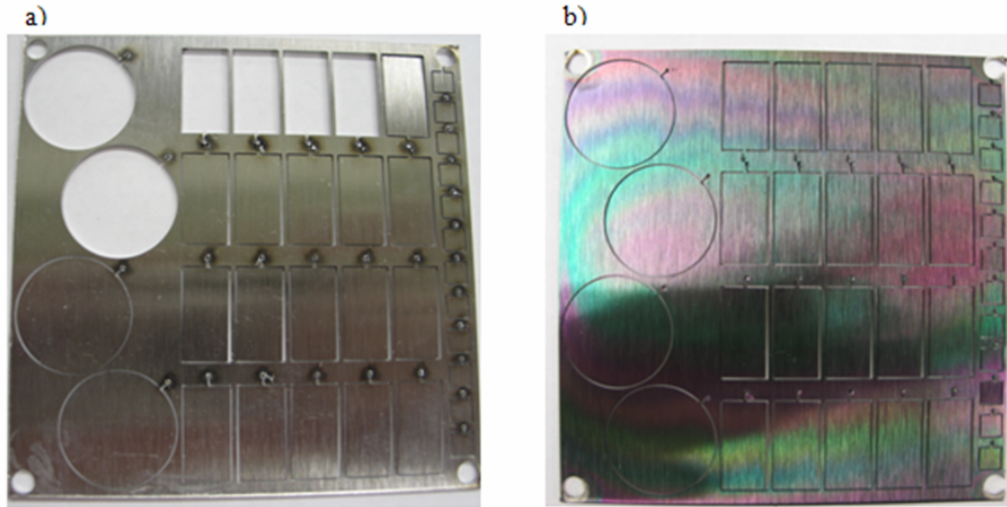
### Metallic Alloy Substrates and Surface Finishes

Several different types of steel alloys were used in this study. Ferritic stainless steels, such as Crofer and commercially-available AISI430 (430SS) were used for SOFC(IC) evaluations, in addition to 440A and 304 steels for complementary thickness, adhesion and composition assessments. The steel surface finishes investigated included:

- air annealed and rough cold-rolled (dull finish with directional roll marks);
- bright annealed (in reducing atmosphere) and fine cold-rolled (mirror-like finish with directional roll marks - less rough);
- bead blasted (very dull, textured finish - roughest); and,
- lapped/polished (mirror-like – smoothest).

Identified as two of the most favorable alloys due to cost, mechanical characteristics, and availability, 430SS and Crofer with different surface finishes were the primary substrates of interest. Substrates were typically square sheets ~100 x 100 x 1mm with laser cut specimen tabs (J.E. Soares – Belgrade, MT) for specific analyses. Figure 3.2 is an image from a typical substrate sheet; showing, a) an uncoated sheet, and b) a coated sheet (note the optical interference pattern associated with thickness variations of the transparent oxide coating). In this case, the ~25mm dia. circular specimen tabs (left) are used for dual atmosphere investigations, the ~10x20mm rectangular specimens (center) are used for surface evaluations including ASR measurements, and the ~5x5mm specimens (right) are for ancillary investigations (discussed further in Chapter 5).

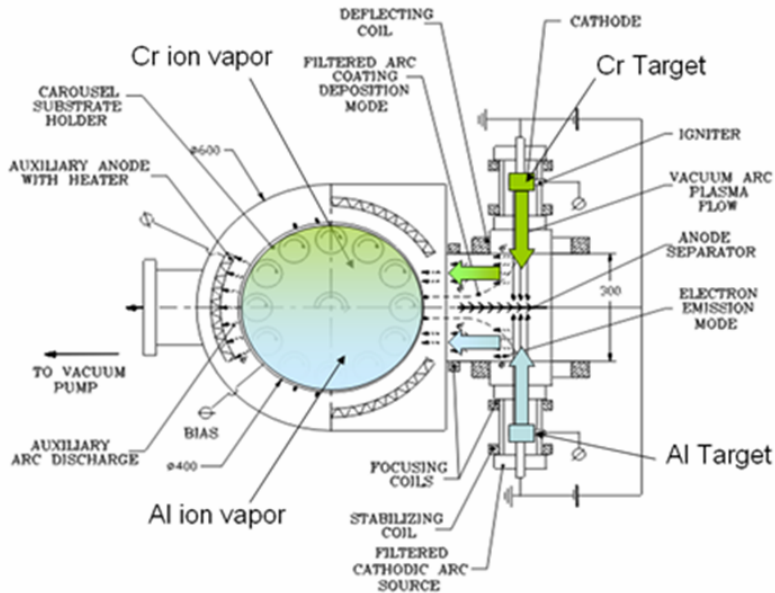
Figure 3.2. 430SS substrate plate (~100 x 100 x 1mm) with laser cut specimen tabs: a) uncoated; b) with 0.5-1.5 $\mu$ m LAFAD TiCoMnCrAlYO coating.



### Arcmac Surface Engineering Facilities and Technology

Arcmac Surface Engineering, LLC (ASE) began its Bozeman, MT research and development operations in 2002, using a patented large area filtered arc (LAFAD) technology to develop functional coatings for several different applications. LAFAD technology utilizes a rectangular cathodic vacuum arc plasma duct with 90° deflecting magnetic field, which draws ions into the deposition chamber, and effectively filters out neutral particles and droplets produced during the vacuum arc evaporation process. A schematic of a typical LAFAD system (top view) is shown in Figure 3.3. In this schematic, the large area filtered arc plasma sources are equipped with Cr and Al metal targets, which are vacuum arc evaporated, creating fully-ionized metal plasma vapors of Cr and Al within the deposition chamber. Gases such as nitrogen and/or oxygen are introduced during the process to react with the metal plasma vapors on substrate surfaces

Figure 3.3. Schematic illustration of Arcomac's large area filtered arc deposition (LAFAD) surface engineering system.

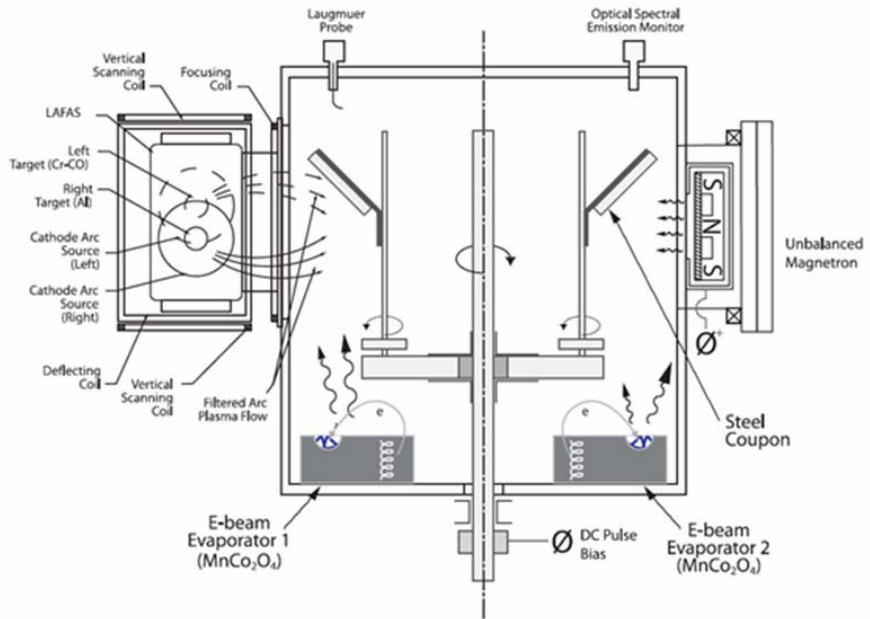


(rotating in front of the LAFAD source) to grow dense, nano-crystalline/amorphous composite ceramic coatings. LAFAD coatings for SOFC(IC) applications began with nitrides, oxinitrides and oxides of aluminum and chromium (arc evaporated metal target materials). The intent was to produce coatings with a combination of diffusion-barrier (e.g., AlN,  $\text{Al}_2\text{O}_3$ ) and electronically conductive (e.g., CrN,  $\text{Cr}_2\text{O}_3$ ) components. Dopant elements intentionally included later into the LAFAD target materials (and thus the deposited coatings) included Y, Ti, Co and Mn. These elements were selected due to the high-temperature stability and electronic conductivity of their respective oxides.

LAFAD technology was also combined with conventional EBPVD technology in a patented hybrid filtered arc plasma source ion deposition (FAPSID) surface engineering system to deposit  $(\text{Co},\text{Mn})_3\text{O}_4$  spinel coatings, in both single segment and layered configurations [ $(\text{Co},\text{Mn})_3\text{O}_4$  serving as the top layer with LAFAD bottom layer – see

Figure 3.1]. This was accomplished by electron beam evaporation of a pre-sintered ceramic target with a nominal composition of  $\text{Co}_{1.5}\text{Mn}_{1.5}\text{O}_4$ . The filtered arc-assisted EBPVD (FA-EBPVD) process is shown schematically (side view) in Figure 3.4. When the LAFAD deflecting electromagnetic field coils are deactivated, the LAFAD source serves as an effective plasmatron, providing significant electron current to the auxiliary anode within the vacuum chamber. The LAFAD plasma flow (absent of LAFAD target ions) ionizes the vapors from the electron beam evaporation process, significantly densifying the resultant surface deposit.

Figure 3.4. Schematic side view of hybrid FA-EBPVD process.  
Note: Unbalanced magnetrons shown were not used in this investigation.



During both the LAFAD and FA-EBPVD processes, a negative bias potential is applied to the substrates to increase the depositing ion energy, resulting in intense ion

bombardment and coating restructuring during the growth process. Although a wide-range of substrate biases were investigated (from 0 to -300V), typically this was set at approximately -40VDC, and pulsed (from 0 to -40V) at ~40kHz.

### MSU Evaluation Facilities

For this SOFC(IC) coating study, several bench-top furnaces were equipped with power supplies and data acquisition systems to oxidize samples and measure time-dependant ASR (in 800°C Bozeman, MT air), a critical SOFC(IC) performance metric. ASR measurement procedures are detailed elsewhere [16,29]. Precision cross sectioning and polishing equipment coupled with state-of-the-art surface analysis techniques permitted unique views into the structure and composition of SOFC(IC) coatings as a function of exposure. Surface analytical techniques included: optical microscopy for surface morphology, thickness and adhesion assessments; x-ray diffraction (XRD) for coating structural composition and phase identification; both LaB<sub>6</sub> filament and field-emission scanning electron microscopy (SEM and FE-SEM) with energy dispersive x-ray spectroscopy (EDS) for elemental composition/distribution and electron backscattering diffraction (EBSD) for microstructure evaluation and crystalline phase identification using automated software for indexing selected area electron diffraction (SAED) Kikuchi patterns; and Rutherford backscattering spectroscopy (RBS) (using a ~2MeV He beam) for quantitative elemental analysis. Cr volatility was also assessed using a novel experimental apparatus in which Cr vapors (from specimens within a tube furnace in 800°C humid air flow) are collected on Si substrates, and subsequently analyzed via RBS.

### Collaborator Evaluation Facilities

Both Pacific Northwest National Laboratory (PNNL) and Lawrence Berkeley National Laboratory (LBNL) graciously provided experience and analytical support. PNNL performed advanced Grazing angle Incidence XRD (GI-XRD), tunneling electron microscopy (TEM) and, high energy RBS ( $\sim$ 4MeV He beam) for increased depth penetration, and nuclear reaction analysis. LBNL measured Cr volatility of coated and uncoated Crofer and 430SS using a transpiration apparatus (800°C humid air flow by a specimen for 24 hours) and induction-coupled mass spectrometry (ICP-MS) of resultant condensates.

## CHAPTER 4

INVESTIGATION RESULTS, OBSERVATIONS  
AND DISCUSSIONSOverview

This chapter highlights results from previously published and as yet unpublished manuscripts regarding SOFC(IC) corrosion behavior of ferritic steels with and without LAFAD and/or FA-EBPVD protective coatings [17,29,57-59]. Table 4.1 reviews LAFAD evaporation target material and reactive gas combinations explored in this study. In total, over 40 unique LAFAD coating processes were investigated for the SOFC(IC) application. In addition, four unique FA-EBPVD  $(Co,Mn)_3O_4$  coatings were applied both

Table 4.1. LAFAD process targets: a) with reactive gas combinations; O, N and M represent processes using oxygen, nitrogen and an oxygen/nitrogen mix respectively, blank cells represent target combinations not yet explored; b) compositions (wt%).

a)

	Reactive Gasses: O( $O_2$ ); N( $N_2$ ) M(Mix)	LAFAD Target 2						
		Cr	Al	CrCo	CoMn	CrAlY	TiCrAlY	CoCrAlY
LAFAD Target 1	Cr	O/NM	O/NM	X	X	0	0	0
	Al	O/NM	O/NM	O/NM	X	0	0	0
	CrCo	X	O/NM	X	X	X	X	X
	CoMn	X	X	X	0	X	0	X
	CrAlY	0	0	X	X	0	0	X
	TiCrAlY	0	0	X	0	0	X	0
	CoCrAlY	0	0	X	X	X	0	X

b)

	LAFAD Target	LAFAD Target Composition (wt%)					
		Cr	Al	Co	Mn	Ti	Y
LAFAD Target	Cr	>99.5	-	-	-	-	-
	Al	-	>99.5	-	-	-	-
	CrCo	85	-	15	-	-	-
	CoMn	-	-	50	50	-	-
	CrAlY	30	69	-	-	-	1
	TiCrAlY	30	48	-	-	20	2
	CoCrAlY	28.5	9.5	61.5	-	-	0.5

directly to uncoated specimens and selected LAFAD pre-coated specimens. Coating deposition process parameter variations resulted in broad experimental matrices. The results presented and discussed here emphasize common SOFC(IC) corrosion behaviors among the investigated coatings. Table 4.2. outlines four single segment LAFAD, one single segment FA-EBPVD, and two layered LAFAD+FA-EBPVD ceramic oxide coatings. In addition to this dissertation, SOFC(IC)-relevant behavior of these and other LAFAD and FA-EBPVD oxide, nitride and oxinitride coatings are reported elsewhere [17,29,57-59]. A summary discussion of LAFAD and FA-EBPVD technologies in the context of SOFC(IC) protective coating research and development is offered in Chapter 5.

Table 4.2. LAFAD and FA-EBPVD coatings; a) single segment LAFAD coating compositions, b) single segment FA-EBPVD coating composition and, c) two segment LAFAD + FA-EBPVD coatings. Note: Elemental compositions (at%) estimated by EDS and/or RBS; coating thicknesses ranged from ~0.3-4.0 $\mu$ m.

a) Single segment LAFAD coating designations, arc evaporation targets and coating compositions

Designation	Target 1	Target 2	Al	Cr	Co	Mn	Ti	Y	O
CrAlYO	CrAlY	Al	30	7	-	-	-	0.5	bal.
CoCrAlYO	CrAlY	CoCrAlY	18	14	12	-	-	0.5	bal.
TiCrAlYO	CrAlY	TiCrAlY	23	13	-	-	3	0.5	bal.
TiCoMnCrAlYO	TiCrAlY	CoMn	12	14	0.5	15	4	0.5	bal.

b) Single segment FA-EBPVD coating designation, evaporation target and composition

Designation	EB Target	Co	Mn	O
(Co,Mn) <sub>3</sub> O <sub>4</sub>	Co <sub>1.5</sub> Mn <sub>1.5</sub> O <sub>4</sub>	22	20	bal.

c) Two segment LAFAD + FA-EBPVD coatings

Bottom Layer LAFAD Coatings	Top Layer FA-EBPVD Coating	
	$\sim 1\mu$ m (Co,Mn) <sub>3</sub> O <sub>4</sub>	
~0.3 $\mu$ m CrAlYO	0.3 $\mu$ m CrAlYO + 1 $\mu$ m (Co,Mn) <sub>3</sub> O <sub>4</sub>	
~2.0 $\mu$ m CrAlYO	2.0 $\mu$ m CrAlYO + 1 $\mu$ m (Co,Mn) <sub>3</sub> O <sub>4</sub>	

### SOFC Interconnect-Relevant Performance

Prohibitive costs associated with full-scale SOFC stack testing often favor materials characterization under simulated conditions. As discussed in Chapters 1 and 2, a primary concern for SOFC(IC)s is the interaction with cathode gas-phase (air) exposure. The SOFC cathode is responsible for the electrochemical reduction of oxygen (creating oxygen anions which transport through the electrolyte). This process requires electrons, which transport through the SOFC(IC) from the anode electrochemical fuel oxidation in the adjacent series-connected cell into the cathode to meet with adsorbed oxygen at the cathode TPB. The SOFC(IC)/cathode interface must therefore retain low and stable ASR. SOFC(IC)/cathode interface degradation is commonly attributed to interaction with oxygen. This study focuses primarily on characteristic interactions of ferritic steel SOFC(IC) surfaces (coated and uncoated Crofer 22 APU and 430SS – Table 4.3) with Bozeman, MT ambient (laboratory) air at ~800°C for varying durations. ASR and Cr volatility measurements were acquired to further assess the SOFC(IC)-relevant performance of (coated and uncoated) ferritic steels.

Table 4.3. Ferritic alloys used in this study (estimated compositions in wt%).

	Fe	Cr	Mn	Si	Cu	P	Ti	La	Mo	S	C
Crofer 22 APU	bal.	22	1	<0.5	<0.5	0.05	0.2	0.2	-	-	<0.03
430SS	bal.	17	0.8	<1.0	-	0.05	-	-	<0.5	<0.03	<0.12

Ancillary investigations consider interactions with cathode materials and dual atmosphere (separating oxidizing/reducing) exposures of coated and uncoated SOFC(IC) alloys, and are discussed further in Chapter 5.

### Surface Oxidation Behavior

Sample specimens of both coated and uncoated ferritic steels were exposed to 800°C laboratory air (with no control of flow or humidity) for varying time intervals up to ~2,000 hours (~80 days). The surface morphology, chemical and phase characteristics were assessed before and after these exposures. Selected results exemplifying common observations are presented, with discussions of SOFC(IC) implications.

Uncoated Specimens Figure 4.1 presents SEM surface images of uncoated (polished) Crofer before and after 800°C air exposure for ~2,000 hours. The TGO scale is comprised of multi-faceted surface crystallites, ranging in characteristic size from submicron up to ~10 $\mu$ m. SEM/EDS/EBSD analyses reveal that the surface crystallites are primarily CrMn<sub>2</sub>O<sub>4</sub> spinel, with a low density of relatively flat Fe-rich crystallites, likely hematite (Fe<sub>2</sub>O<sub>3</sub>). As mentioned in Chapter 2, the TGO scale on Crofer 22APU evolves a layered stratigraphy, with a CrMn<sub>2</sub>O<sub>4</sub> spinel-based surface (top) layer and Cr<sub>2</sub>O<sub>3</sub> corundum-based bottom layer. The SEM/EDS elemental mapping cross section in Figure 4.2. illustrates this stratigraphy on Crofer 22APU specimen exposed to 800°C air for ~750 hours (Cr = Red, Mn = Green and Pt = Blue [Pt present from ASR testing]). The TGO stratification is likely due to the high oxygen affinity of Mn, and relative

stability of its oxides compared with Cr. Subsequent to stratification, continued TGO scale growth appears dominated by the  $\text{Cr}_2\text{O}_3$ -based bottom layer thickening.

Figure 4.1. Crofer 22APU (lap/polished surface); before (a) and, after (b) 2,000 hours in 800°C air.

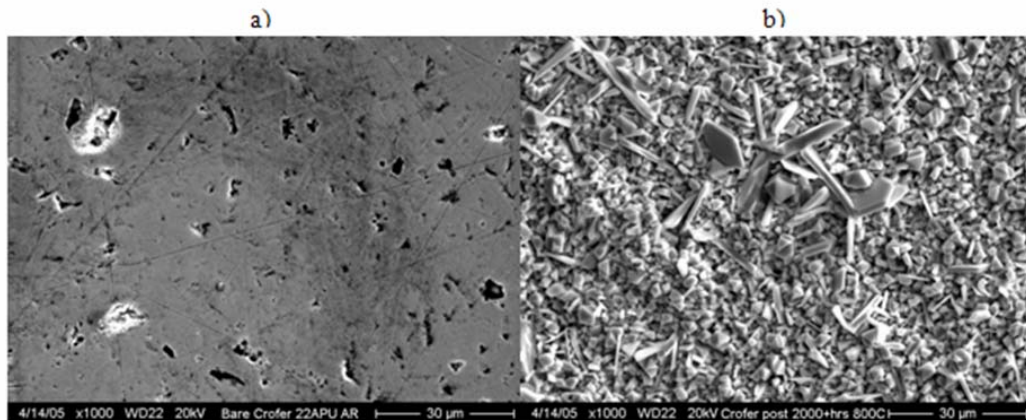
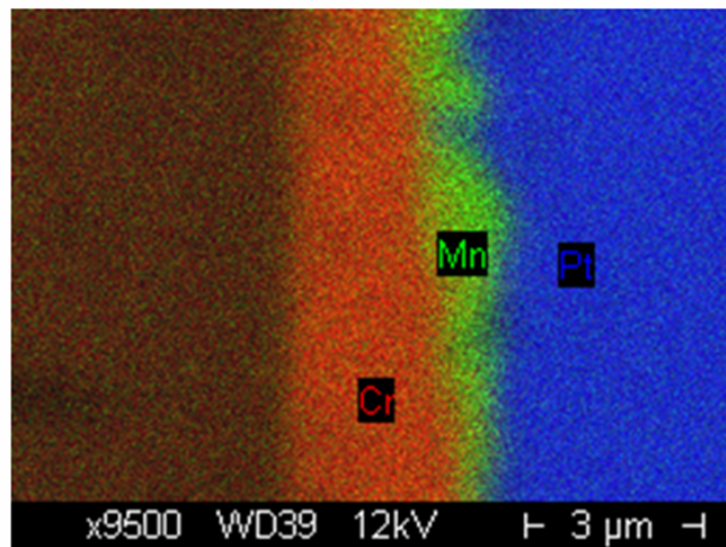
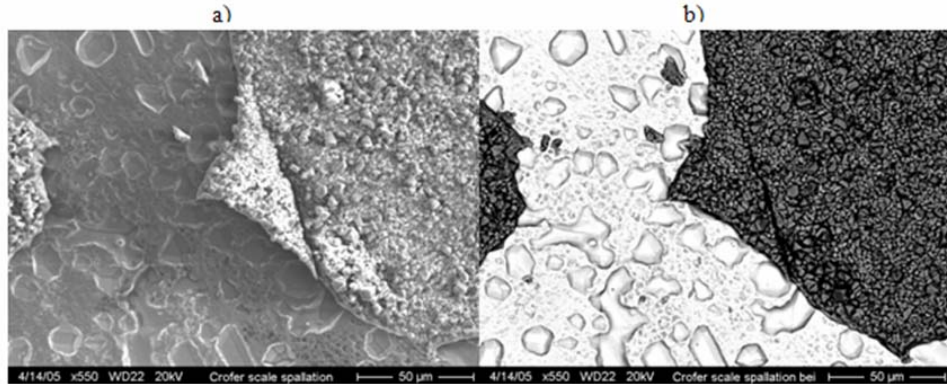


Figure 4.2. EDS elemental map of TGO scale formed on Crofer 22APU after ~750hours in 800°C air.



Continued TGO scale growth results in stress energy accumulation and eventual relief in the form of scale debonding. This phenomena is illustrated in Figure 4.3, which presents SEM secondary and backscattered electron images contrasting the compromised TGO scale and underlying Crofer 22APU substrate after a ~2,000 hour exposure to 800°C air. The TGO scale thickness was estimated at ~6-10 $\mu\text{m}$  and only localized debonding was observed; however, this instability would seem to limit SOFC(IC) durability of uncoated Crofer 22 APU when operated at 800°C.

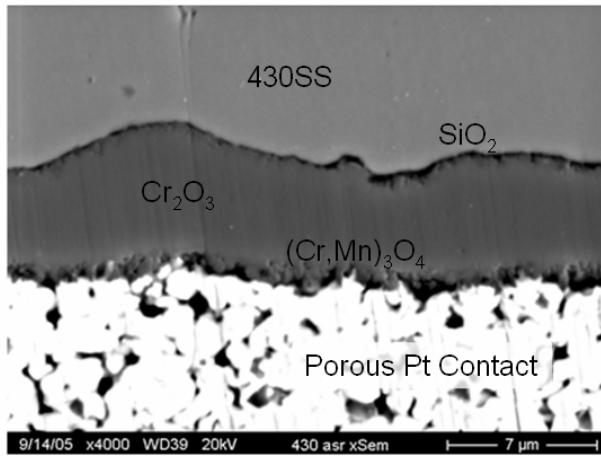
Figure 4.3. SEM images of spontaneous spallation of TGO scale grown on Crofer 22APU after 2,000 hours oxidation in 800°C air: (a) secondary electron image; (b) backscattered electron image providing contrast between metal (bright) and oxide (dark).



Similar oxidation behavior is observed with uncoated 430SS, although lower bulk Cr concentrations compared to Crofer 22 APU (~17% vs. ~22%) leads to the oxidation of other alloy (or impurity) elements, such as Si. This may increase TGO scale ASR and further deteriorate SOFC(IC) performance. An SEM cross section of uncoated 430SS after ~1,000 hours ASR testing is shown in Figure 4.4. The total TGO scale thickness is ~6 $\mu\text{m}$  and is comprised of a thin Mn-rich surface layer (likely  $(\text{Cr}, \text{Mn})_3\text{O}_4$ ),  $\text{Cr}_2\text{O}_3$  based bottom layer, and Si-rich oxides (e.g.,  $\text{SiO}_2$ ) at the interface with the underlying steel. Formation of  $\text{SiO}_2$  in addition to observed localized TGO scale debonding at the

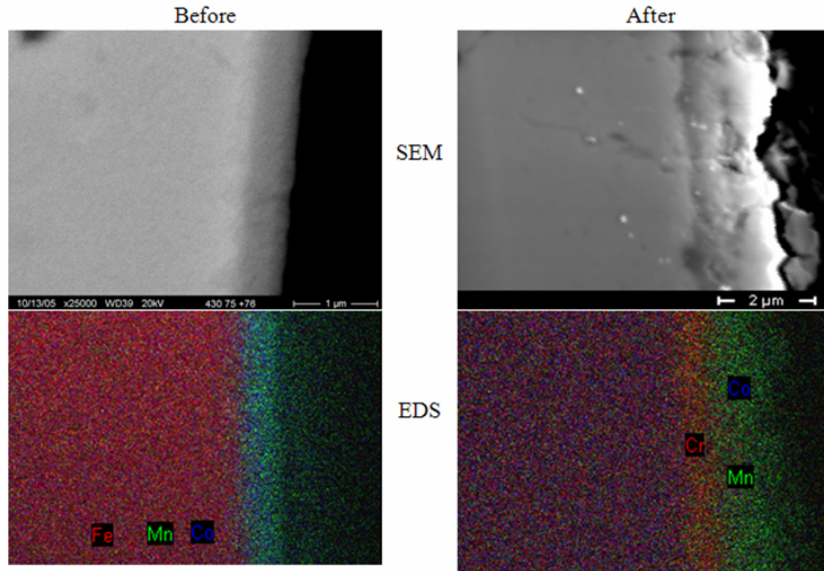
scale/alloy interface may substantially increase ASR. In general, these and other published observations indicate limited durability of uncoated ferritic steel SOFC(IC)s at 800°C [14].

Figure 4.4. SEM cross section image of 430SS after ~1,000 hours ASR testing in 800°C air.



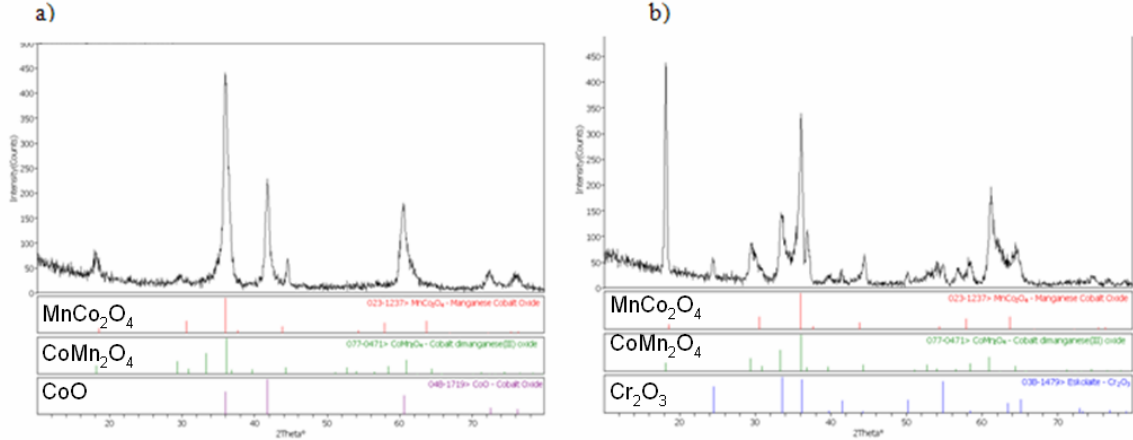
Coated Specimens Figures 4.5 presents SEM images and corresponding EDS elemental mappings from a  $\sim 1.0\mu\text{m}$  FA-EBPVD  $(\text{Co},\text{Mn})_3\text{O}_4$  coating (Table 4.2.b) on 430SS before and after  $\sim 100$  hours in 800°C air. During this exposure, oxygen has effectively transported through the  $(\text{Co},\text{Mn})_3\text{O}_4$  coating, resulting in the formation of a  $\sim 0.5\mu\text{m}$   $\text{Cr}_2\text{O}_3$ -based TGO layer at the metal/coating interface. As the  $(\text{Co},\text{Mn})_3\text{O}_4$  coating is observed to be fully dense, solid-state oxygen transport must occur within the coating, e.g., oxygen vacancy and/or grain boundary transport.

Figure 4.5.  $\sim 1\mu\text{m}$  FA-EBPVD  $(\text{Co},\text{Mn})_3\text{O}_4$  coated 430SS before and after  $\sim 100$  hours in  $800^\circ\text{C}$  air.



The formation of the  $\text{Cr}_2\text{O}_3$ -based TGO sublayer is further confirmed in GI-XRD patterns shown in Figure 4.6, which are presented for the coating as-deposited (Figure 4.6a) and subsequent to  $\sim 100$  hours in  $800^\circ\text{C}$  air (Figure 4.6b). Using Jade software, GI-XRD pattern indexing and analyses (including ferritic steel substrate subtraction) reveals that the coating as-deposited is a composite of nanocrystalline  $\text{CoO}$ ,  $\text{CoMn}_2\text{O}_4$  and  $\text{MnCo}_2\text{O}_4$  spinels embedded into an otherwise amorphous matrix [17]. After the 100 hour  $800^\circ\text{C}$  air exposure,  $\text{Cr}_2\text{O}_3$  XRD peaks are detected,  $\text{CoMn}_2\text{O}_4$  and  $\text{MnCo}_2\text{O}_4$  peaks have sharpened (crystallite growth) and the  $\text{CoO}$  peak has vanished (likely transforming into one of the Co-containing spinels). This observation agrees well with both the SEM/EDS observations above and a published pseudo-binary phase diagram for  $\text{Mn}_3\text{O}_4$  and  $\text{Co}_3\text{O}_4$ , which shows  $(\text{Co},\text{Mn})_3\text{O}_4$  spinel stability in most of the compositional range at  $800^\circ\text{C}$  [61].

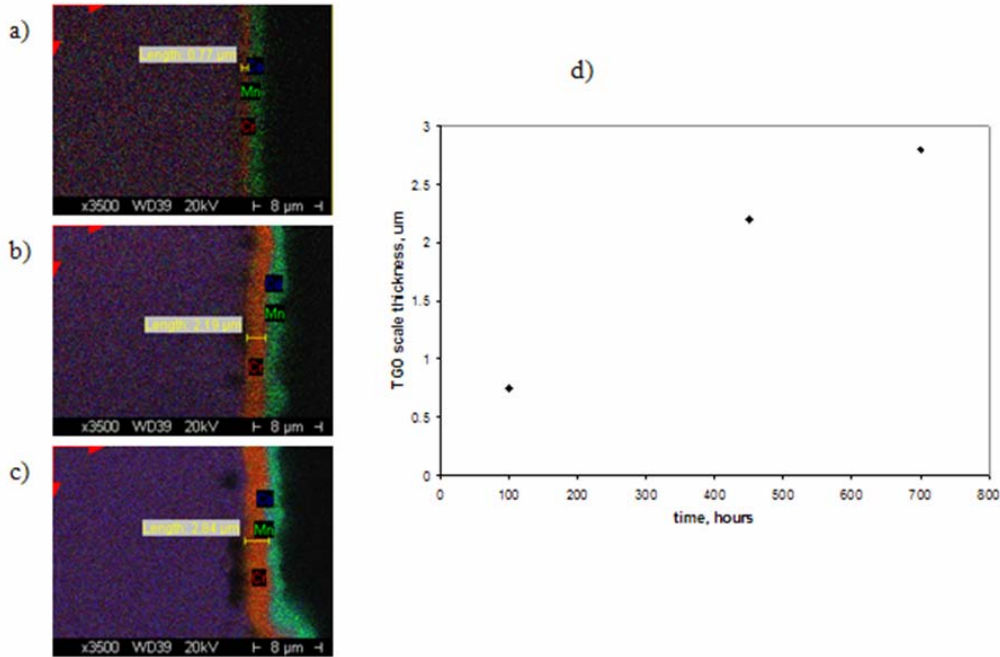
Figure 4.6. GI-XRD patterns for a  $\sim 1.0\mu\text{m}$  FA-EBPVD  $(\text{Mn},\text{Co})_3\text{O}_4$  coating on 430SS: a) as-deposited; b) subsequent 100 hours oxidation in air at  $800^\circ\text{C}$ .



In  $800^\circ\text{C}$  air, continued TGO growth is observed below the  $(\text{Co},\text{Mn})_3\text{O}_4$  coating, as shown in the cross section EDS elemental mapping and estimated TGO scale thickness vs. time graph in Figure 4.7. TGO scale thickness reaches  $\sim 2.8\mu\text{m}$  during the  $\sim 700$  hour,  $800^\circ\text{C}$  air exposure. Compared with the  $\sim 6\mu\text{m}$  TGO scale observed on the uncoated 430SS after  $\sim 1,000$  hours, the thin ( $\sim 1\mu\text{m}$ )  $(\text{Co},\text{Mn})_3\text{O}_4$  coating appears to provide some limited barrier against oxygen transport, although even at this reduced growth rate, TGO scale thickness would be substantial at 40,000 hours, and would likely prematurely debond, or exhibit prohibitively high ASR.

Assuming constant oxygen diffusivity in the FA-EBPVD  $(\text{Co},\text{Mn})_3\text{O}_4$  coating, increasing its thickness would decrease oxygen transport and reduce TGO scale growth. Recently,  $\sim 20\mu\text{m}$   $(\text{Co},\text{Mn})_3\text{O}_4$  coatings (deposited on Crofer 22 APU and 430SS using conventional techniques) have been reported to demonstrate stable performance in  $800^\circ\text{C}$  air for  $>1$  year ( $\sim 9,200$  hours), with a  $\sim 4\mu\text{m}$  TGO scale observed under the coating, compared with a  $\sim 14\mu\text{m}$  TGO scale on uncoated Crofer 22 APU [60]. Low ASR values

Figure 4.7. Cross section EDS elemental maps of  $\sim 1.0\mu\text{m}$  FA-EBPVD  $(\text{Co},\text{Mn})_3\text{O}_4$  after: a)  $\sim 100$ ; b)  $\sim 450$ ; and, c)  $\sim 700$  hours in  $800^\circ\text{C}$  air; and, d) plot of estimated TGO scale thickness as a function of time.



for this coating after the year exposure were also observed [60]. Results from the same study using 430SS were less promising with the observed formation of insulating silicon oxide at the steel/TGO scale interface. This was attributed to continued oxygen transport through the  $\sim 20\mu\text{m}$   $(\text{Co},\text{Mn})_3\text{O}_4$  coating and Cr surface depletion in the 430SS, resulting in non-protective  $\text{Cr}_2\text{O}_3$  [60]. By impeding oxygen transport, protective coatings effectively decrease oxygen activity at the substrate surface, preventing oxidation of minor alloying elements, i.e., Si. However, if the coating is insufficient in blocking oxygen diffusion and/or protective alloying elements within the substrate are deficient, oxides of minor alloying elements will form and grow.

It is generally understood that high-temperature electronic conductivity in ceramic oxides, such as  $(\text{Co},\text{Mn})_3\text{O}_4$  and other spinels and perovskites may be explained (in-part)

by high defect concentration, e.g., oxygen vacancies, which are compensated via conduction electrons,

$$O_O^x = V_O^- + 2e' + 1/2O_2 \quad (4.1).$$

This feature also facilitates anion conductivity (via vacancy transport), permitting continued oxygen permeability. Ceramic oxide coatings exhibiting anion-dominant transport (during high-temperature corrosion) permit TGO scale formation and growth beneath the coating (see Figure 4.5). During long-term exposures, this may lead to coating/TGO failure, or otherwise unacceptable SOFC(IC) performance.

To improve the SOFC(IC) performance of oxygen permeable cermamic oxide coatings, such as  $(Co,Mn)_3O_4$ , a layered approach may be useful (Figure 3.1.c and Table 4.2.c). In this structure, an adhesion-promoting, diffusion-barrier LAFAD Cr/Al oxide-based coating, intended to inhibit ionic transport, is deposited prior to the FA-EBPVD  $(Co,Mn)_3O_4$  layer. Figure 4.8 presents SEM images and corresponding EDS elemental mappings from a  $\sim 2.0\mu m$  LAFAD CrAlYO bottom layer coating with a  $\sim 1.0\mu m$  FA-EBPVD  $(Co,Mn)_3O_4$  top layer coating on 430SS before and after  $\sim 300$  hours in  $800^\circ C$  air. It appears some interdiffusion between the top/bottom coating and coating/steel interfaces occurs during this exposure; however, the formation of a distinct TGO is not observed. The dimensional and chemical stability during this exposure may be attributed to the relatively thick amorphous/nano-crystalline alumina-based diffusion-barrier bottom layer coating. The LAFAD CrAlYO bottom layer coating has also been shown to promote adhesion of the FA-EBPVD  $(Co,Mn)_3O_4$  upper layer [17]. Further discussions regarding LAFAD Cr/Al oxide-based coatings and their modifications are provided later.

Figure 4.8. SEM images and corresponding EDS elemental mappings from a  $\sim 2.0\mu\text{m}$  LAFAD CrAlYO bottom layer coating with  $\sim 1.0\mu\text{m}$  FA-EBPVD  $(\text{Co},\text{Mn})_3\text{O}_4$  coating on 430SS before and after  $\sim 300$  hours in  $800^\circ\text{C}$  air.

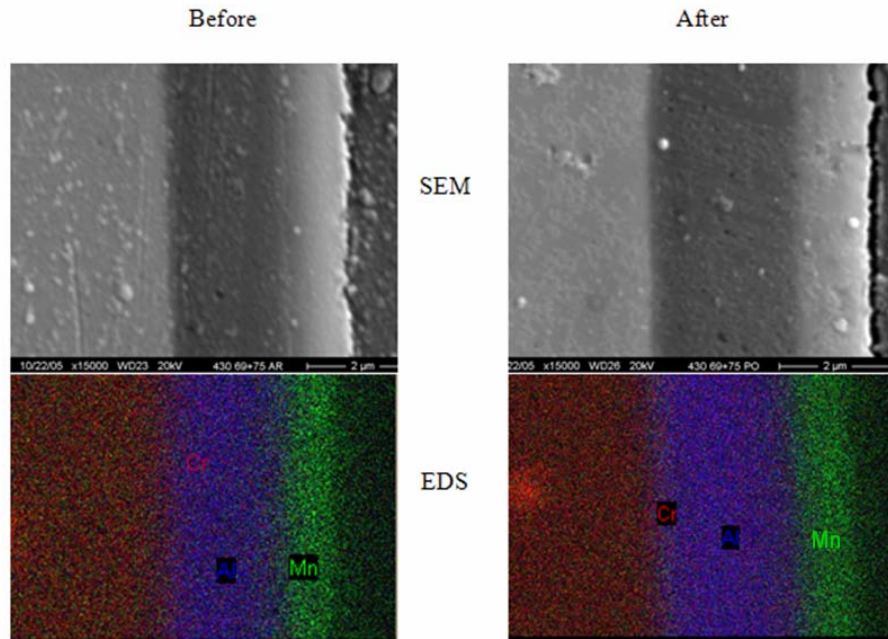
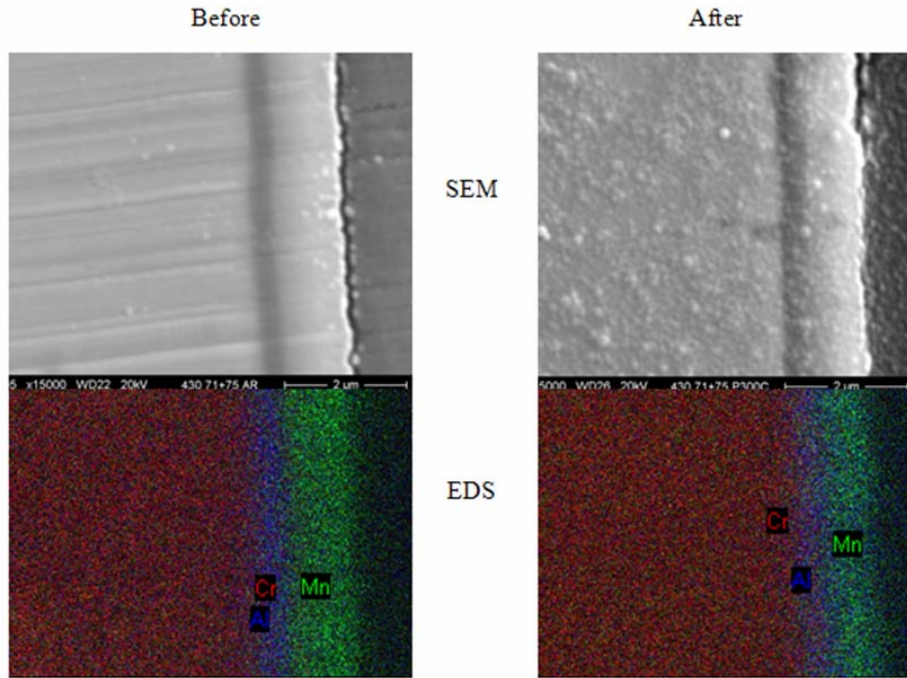


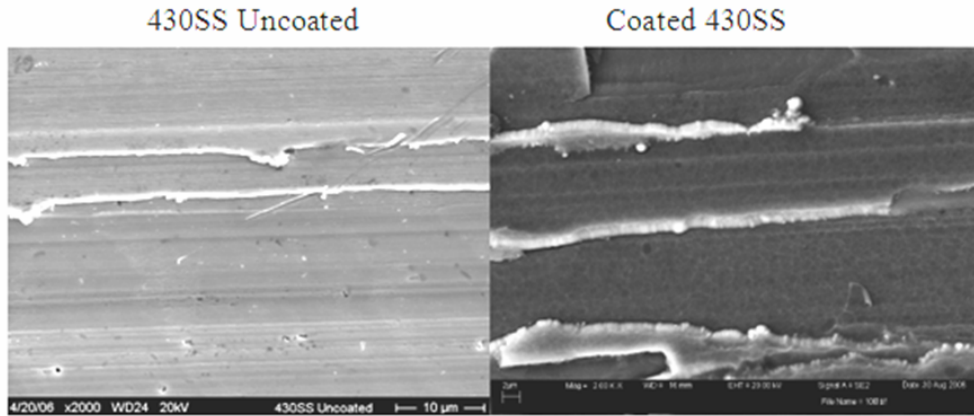
Figure 4.9 presents SEM images and corresponding EDS elemental mappings from a much thinner,  $\sim 0.3\mu\text{m}$  LAFAD CrAlYO bottom layer coating with a  $\sim 1.0\mu\text{m}$  FA-EBPVD  $(\text{Co},\text{Mn})_3\text{O}_4$  top layer coating on 430SS before and after  $\sim 300$  hours in  $800^\circ\text{C}$  air. Similar interdiffusion behavior compared to the thicker bottom layer (Figure 4.8) is observed. Considering the thinness of the LAFAD CrAlYO ( $\sim 0.3\mu\text{m}$ ), its stability and oxygen diffusion-barrier capacity may be compromised during long-term exposures, although ASR behavior is significantly more favorable compared with the thicker bottom layer, as presented latter.

Figure 4.9. SEM images and corresponding EDS elemental mappings from a  $\sim 0.3\mu\text{m}$  LAFAD CrAlYO bottom layer coating with  $\sim 1.0\mu\text{m}$  FA-EBPVD  $(\text{Co},\text{Mn})_3\text{O}_4$  coating on 430SS before and after  $\sim 300$  hours in  $800^\circ\text{C}$  air.



Several variations of the single segment LAFAD CrAlYO coating layers described above have been investigated (Table 4.2.a). Figure 4.10 displays SEM surface images of uncoated 430SS next to a  $\sim 2.0\mu\text{m}$  LAFAD TiCrAlYO coated 430SS. It appears the substrate steel surface topology propagates through the coating, leaving directional finishing marks (terraces) visible on the coating surface.

Figure 4.10. SEM surface images of uncoated and ( $\sim 2.0 \mu\text{m}$  LAFAD TiCrAlYO) coated 430SS.



During  $800^\circ\text{C}$  air exposures, these regions effectively give rise to outward transport of heterovalent, high oxygen affinity Mn cations from the steel. This effect is illustrated in Figure 4.11, which shows SEM images of the  $\sim 2 \mu\text{m}$  LAFAD TiCrAlYO coating surface on 430SS before and after  $\sim 1,200$  hours in  $800^\circ\text{C}$  air at different magnifications. Mn-rich surface crystallites are concentrated at the steel surface roll marks (terraces). In areas away from these roll marks, the coating has remained amorphous, which is shown in more detail in Figure 4.12. The froth-like surface appearance in the magnified SEM images in Figure 4.12 is characteristic of the amorphous LAFAD Cr/Al oxide-based coatings.

Additional evidence for the stability of the amorphous phase and localized Mn-rich surface crystallite formation/growth is shown in Figure 4.13, which presents SEM images with overlaying EBSD SAED Kikuchi patterns from the surface crystallite (indexed as  $(\text{Cr},\text{Mn})_3\text{O}_4$  spinel) and the amorphous/nano-crystalline LAFAD TiCrAlYO coating region (no pattern), before and after 1,200 hours in  $800^\circ\text{C}$  air.

Figure 4.11. SEM surface images of  $\sim 2.0\mu\text{m}$  LAFAD TiCrAlYO coated 430SS before and after  $\sim 1,200$  hours in  $800^\circ\text{C}$  air.

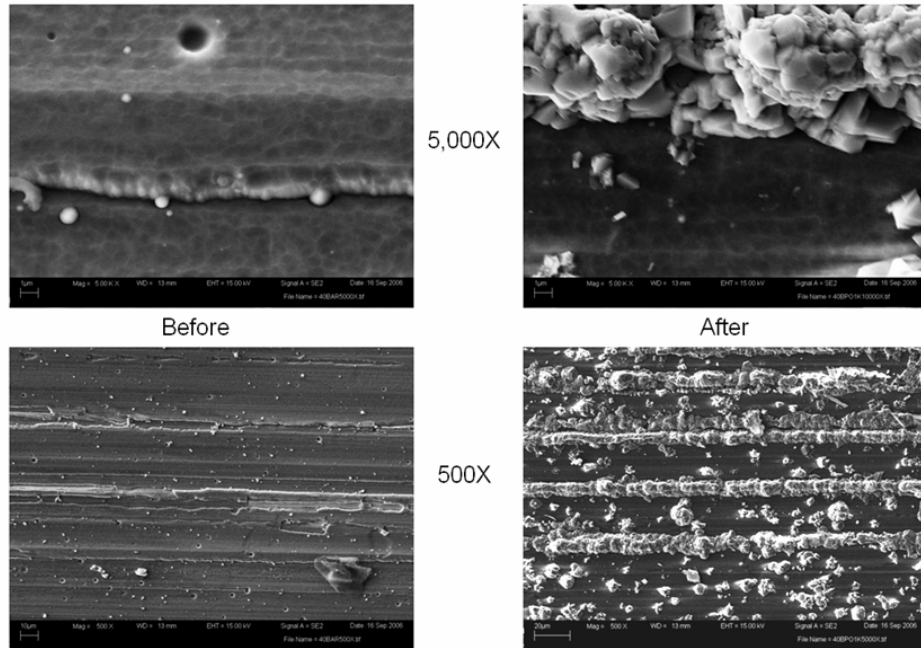


Figure 4.12. SEM images of  $\sim 2\mu\text{m}$  LAFAD TiCrAlYO coated 430SS amorphous/nano-crystalline coating regions before and after 1,200 hours in  $800^\circ\text{C}$  air.

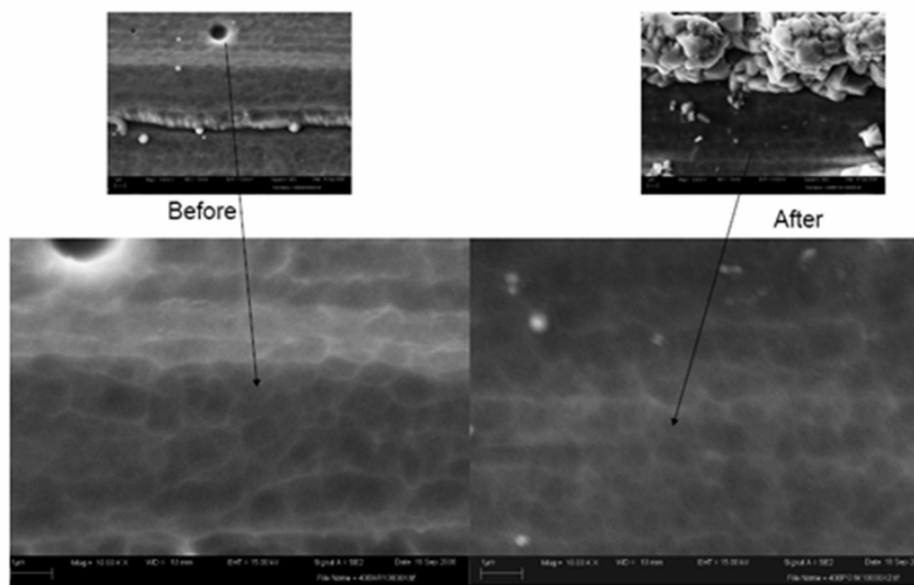
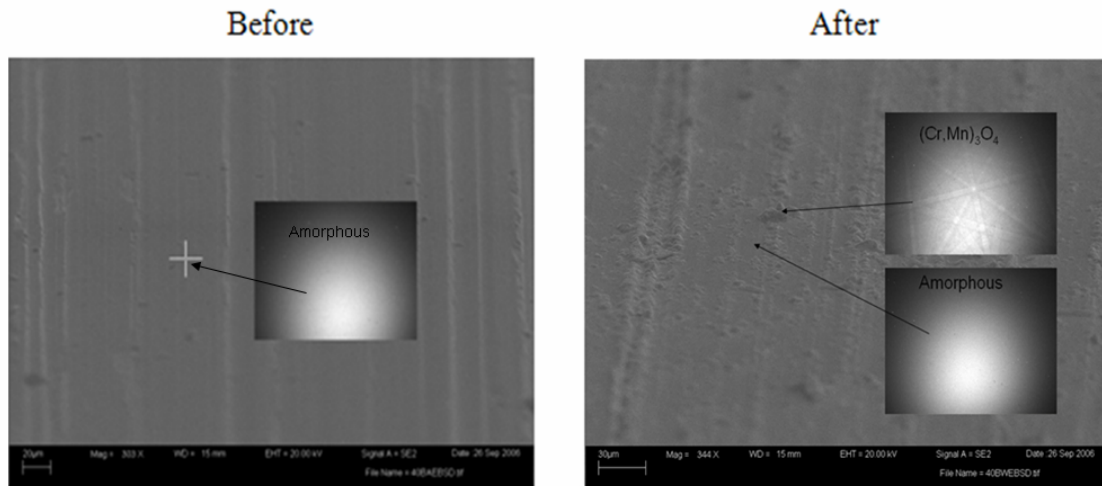


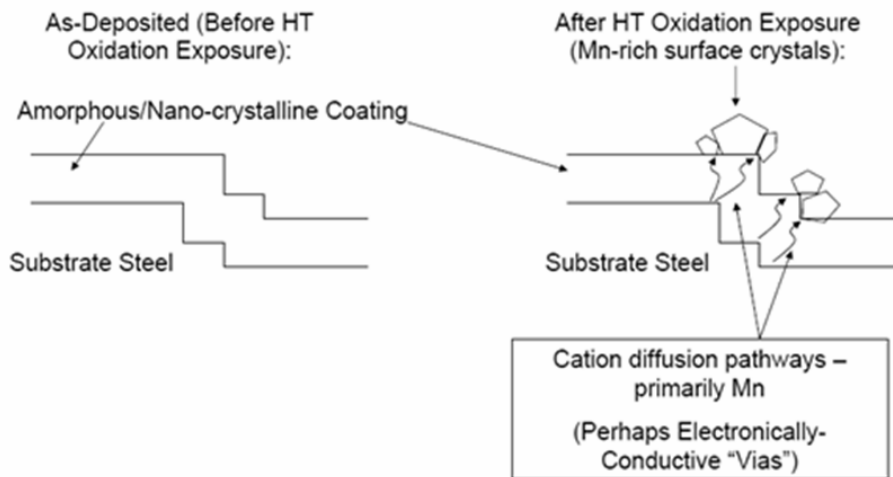
Figure 4.13 SEM images with EBSD Kikuchi SAED patterns of a  $\sim 2.0\mu\text{m}$  LAFAD TiCrAlYO coating before and after  $\sim 1,200$  hours in  $800^\circ\text{C}$  air.



The thermal stability of the amorphous/nano-crystalline TiCrAlYO coating thus seems heavily influenced by the underlying steel surface finish. Given a constant surface energy in a material, large surface area features (e.g., terraces) will result in localized high-energy regions. As the LAFAD coating grows, these regions may be considered local sinks for high-energy features (vacancy defects, etc.) within the predominantly amorphous coating structure. Perturbed regions in the coating (surface features) appear to exhibit higher cation transport rates than areas of the coating away from these features. Mn is known to have a high oxygen affinity, and is uniformly identified in the observed surface crystallites. Outward Mn and/or Cr cation transport from the steel through the coating may react with oxygen (and perhaps Cr in coating) to form the localized  $(\text{Cr},\text{Mn})_3\text{O}_4$  surface crystallites. The localized heterovalent cationic transport pathways may provide electronically conductive pathways through the otherwise semi-conducting/insulating Cr/Al oxide-based amorphous/nano-crystalline coating. This

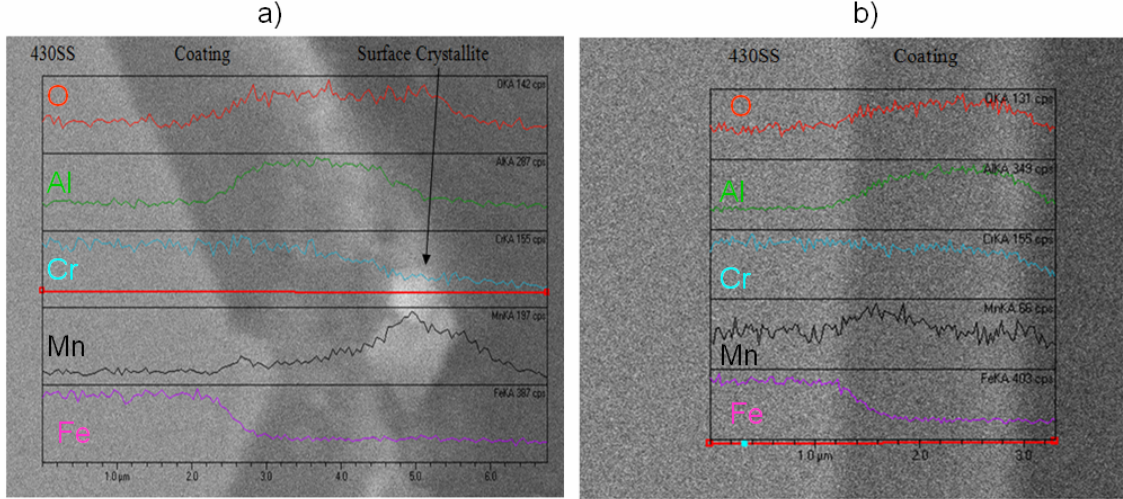
phenomena is schematically illustrated in Figure 4.14. The electronically-conductive pathway evolution may help explain the consistently observed initial ASR decrease with time in these coatings (discussed latter - see Figures 4.17,4.18).

Figure 4.14 Schematic illustration of surface finish and influence on coating evolution during high temperature oxidizing exposures.



The cross section SEM image with overlapping EDS elemental linescan in Figure 4.15 further demonstrates the outward transport propensity of Mn (through a  $\sim 2.0\mu\text{m}$  LAFAD TiCrAlYO coating at a steel roll mark feature after  $\sim 1,200$  hours at  $800^\circ\text{C}$ ). The Mn concentration is elevated in the coating relative to the steel and shows a distinct  $\sim 1\mu\text{m}$   $(\text{Cr},\text{Mn})_3\text{O}_4$  surface crystallite in Figure 15a. A similar image in Figure 4.15b shows an unperturbed coating region after the 1,200 hour  $800^\circ\text{C}$  air exposure. There is also an observed Mn presence within the coating (above the Mn concentration in the steel); however, this has not resulted in the formation of surface crystallites (after 1,200 hours), as in the perturbed region presented in Figure 4.15a.

Figure 4.15. Cross section SEM image with overlaying EDS elemental linescan from a  $\sim 2\mu\text{m}$  LAFAD TiCrAlYO coating after  $\sim 1,200$  hours in 800C air: a) at roll mark area; b) at smooth surface area.



Many TGO scale ceramic oxides, such as  $\text{Cr}_2\text{O}_3$ , exhibit significant cation vacancy concentrations [68]. As in Equation 4.1, cation vacancy defects are also compensated by charge carriers (holes) but in somewhat different fashion,

$$1/2\text{O}_2 = \text{O}_o^X + 3h + V_{\text{Cr}}^{'''} \quad (4.2).$$

Here, an oxygen ion is created at an oxygen lattice site, and a Cr ion vacancy with an effective triple negative charge is balanced by three electron holes.  $\text{Cr}_2\text{O}_3$  exhibits p-type electronic conductivity, with small polaron hopping transport considered the dominant mechanism [62]. The conductivity mechanisms through the LAFAD Cr/Al oxide-based coatings have not been fully characterized, but do appear to exhibit limited cation conductivity, and therefore may exhibit some p-type conductivity.

Crystalline  $\text{Cr}_2\text{O}_3$  and  $\text{Al}_2\text{O}_3$  share the same basic crystal structure, termed corundum or sesquioxide. In this structure, the relatively large oxygen anions form a

hexagonal close pack configuration, leaving the cations to occupy two-thirds of the central octahedral positions. Several different distinct crystalline phases are observed depending upon the cation spatial distribution.  $\text{Cr}_2\text{O}_3$  and  $\text{Al}_2\text{O}_3$  are known to form solid solutions in most of the compositional range, and exhibit regular solution behavior (significantly lower free energy together than apart). This is discussed further later in the context of Cr volatility.

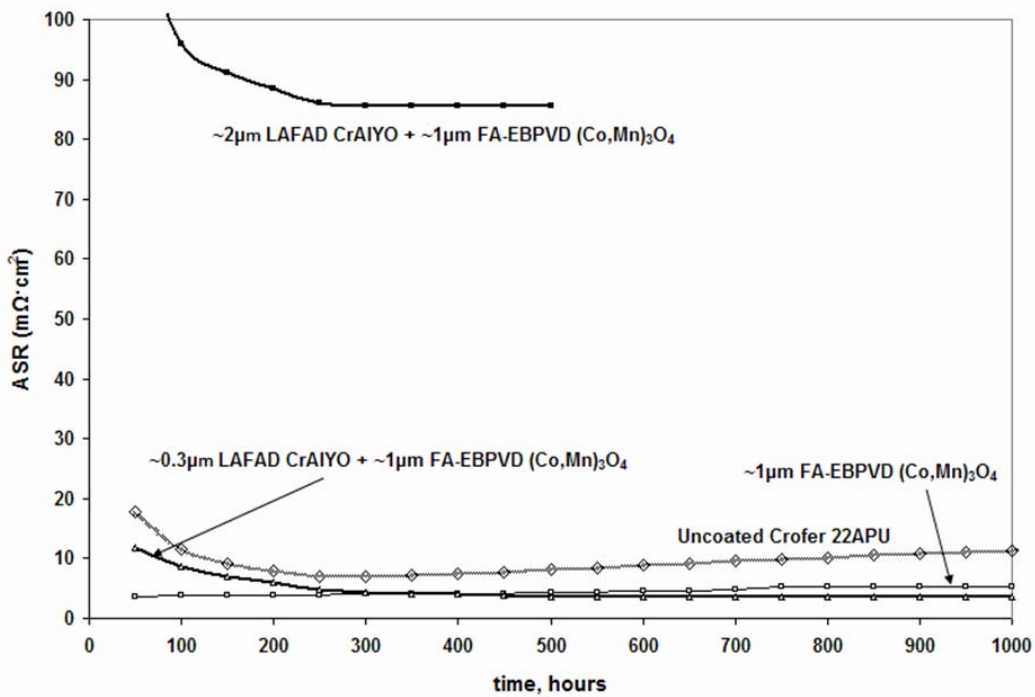
During the LAFAD ceramic oxide coating process, amorphous structures may result due to rapid quenching of plasma vapors into the solid-state. This may effectively “freeze” the depositing ions into position, rather than allowing them to order in more thermodynamically-favored (crystalline) lattice positions. The long-term (>1,200 hours) high-temperature (800°C air) stability of this amorphous state may be afforded (in-part) by the presence of dopant elements, e.g., Y and/or Ti. These species likely form their respective oxides ( $\text{Y}_2\text{O}_3$  and/or  $\text{TiO}_2$ ) which may inhibit recrystallization or crystalline growth by serving as insoluble boundaries between  $(\text{Al,Cr})_2\text{O}_3$  regions, which might otherwise crystallize and grow. LAFAD coating processes which included Co and Mn (Table 4.2) exhibited similar stabilities of their amorphous content; some with higher electronic conductivity, as discussed in the following section.

### Area Specific Resistance

Figure 4.16 presents summary ASR data for coated and uncoated Crofer 22 APU (layered coatings discussed above, Table 4.2.c). After an initial decrease, the uncoated Crofer 22 APU TGO scale ASR increases throughout the 1,000 hour test period. The initial decrease may be related (in-part) to the TGO scale compositional stratification

(due to outward heterovalent Mn cation transport), while the following steady increase can be attributed to continued TGO scale growth (dominated by  $\text{Cr}_2\text{O}_3$ ). Considering parabolic ASR growth after the minimum value, projected ASR at 40,000 is  $\sim 100 \text{ m}\Omega\cdot\text{cm}^2$ , which is the maximum value for the SOFC(IC) application. However, other deleterious effects of continued TGO scale growth (spallation, cathode degradation, etc.) may prohibit the use of uncoated Crofer as an SOFC(IC) material at 800°C. At lower temperatures (e.g.,  $<700^\circ\text{C}$ ), uncoated Crofer may satisfy long-term SOFC(IC) functional requirements.

Figure 4.16. Summary ASR data from Crofer 22 APU with and without coatings, in 800°C air.



The lowest initial ASR observed in Figure 4.16 is of a single layer  $\sim 1.0\text{ }\mu\text{m}$  FA-EBPVD  $(\text{Co,Mn})_3\text{O}_4$  coated Crofer. The ASR for this specimen increases similarly to that of uncoated Crofer; however, at a significantly slower rate. This is presumably due

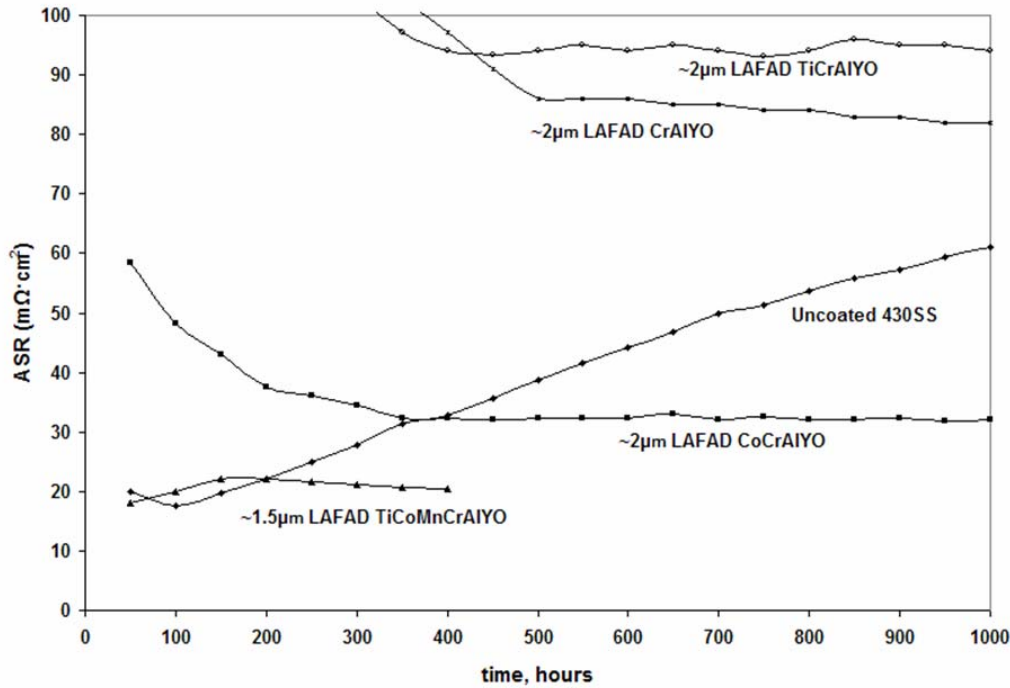
to retarded TGO scale growth beneath the  $\sim 1.0\mu\text{m}$  FA-EBPVD  $(\text{Co},\text{Mn})_3\text{O}_4$  coating. As discussed previously in this chapter, coatings permeable to oxygen will slow but not block continued TGO scale growth. During extended exposures, this may compromise SOFC(IC) coating/TGO scale adhesion due to excessive thickness and associated stress energy.

The layered (LAFAD + FA-EBPVD) coated Crofer specimens exhibit slowly decreasing, followed by stable ASR values during the 1,000 hour test. The specimen with thinner ( $\sim 0.3\mu\text{m}$ ) LAFAD CrAlYO bottom layer ( $\sim 1.0\mu\text{m}$  FA-EBPVD  $(\text{Co},\text{Mn})_3\text{O}_4$  top layer) coating exhibits the lowest ASR, which decreases to and remains below  $\sim 5\text{ m}\Omega\cdot\text{cm}^2$  throughout the experiment. The thicker ( $\sim 2.0\mu\text{m}$ ) LAFAD CrAlYO bottom layer ( $\sim 1.0\mu\text{m}$  FA-EBPVD  $(\text{Co},\text{Mn})_3\text{O}_4$  top layer) coating exhibits the highest ASR, which decreases to a stable  $\sim 85\text{ m}\Omega\cdot\text{cm}^2$  during a  $\sim 500$  hour test. The initial ASR decrease observed with the layered coatings may be explained by layer interdiffusion and interaction with the 430SS substrate (e.g., slow outward heterovalent Mn cation transport). Initially decreasing ASR values were consistently observed for the LAFAD coatings on both Crofer 22 APU and 430SS. ASR stability can be attributed to the diffusion-barrier properties of the LAFAD CrAlYO layer, as shown in Figure 4.16.

Figure 4.17. presents summary ASR data for several coated and uncoated 430SS specimens (single layer LAFAD coatings discussed above, Table 4.2a). ASR behavior of uncoated 430SS was similar to that of uncoated Crofer 22 APU (initial slow decrease followed by continual increase) except the minimal ASR value was higher than that of Crofer ( $\sim 17$  vs.  $7\text{ m}\Omega\cdot\text{cm}^2$ ), and the subsequent ASR increase was more rapid, reaching

$>50 \text{ m}\Omega\cdot\text{cm}^2$  during the 1,000 hour test. The improved ASR behavior in Crofer 22 APU vs. 430SS may be explained by higher Cr content and other engineered alloying elements (e.g., Mn, La, Ti, and low Si) in Crofer 22 APU, which permits formation of a more continuous (protective), low ASR TGO scale. Prohibitively high ASR may alone limit uncoated 430SS for the SOFC(IC) application at 800°C. Lower operation temperatures may permit its use, and should be investigated.

Figure 4.17. Summary ASR data from 430SS with and without coatings, in 800°C air.



ASR values for four LAFAD coated and one uncoated 430SS in Figure 4.17 illustrates the significance of dopant elements within the amorphous/nano-crystalline Cr/Al ceramic oxide coatings. While stability for the amorphous structure may be enhanced by uniformly-present Y (e.g.,  $\text{Y}_2\text{O}_3$  may segregate to boundaries between

locally-organized [quasi-crystalline –  $(\text{Cr},\text{Al})_2\text{O}_3$  regions]), Ti, Co and Mn additions are observed to substantially influence ASR. This effect is more significant with Co and Mn, compared with Ti, which may be attributed to the relatively high electronic conductivity of their respective oxides (e.g.,  $\sigma_{\text{Co}_3\text{O}_4}$  and  $\sigma_{\text{Mn}_3\text{O}_4} > \sigma_{\text{TiO}_2}$ ). ASR of the LAFAD CrAlYO and TiCrAlYO coatings decreases from  $>100 \text{ m}\Omega\cdot\text{cm}^2$  and stabilizes at  $\sim 90 \text{ m}\Omega\cdot\text{cm}^2$  during the 1,000 hour test. The initial decrease is likely due to the effect discussed above and illustrated in Figures 4.11 – 4.15. Heterovalent, high oxygen affinity Mn cations are expected to transport outward from the 430SS through defect-concentrated regions in the coating, forming  $(\text{Cr},\text{Mn})_3\text{O}_4$  surface crystallites and perhaps providing highly conductive electronic transport pathways through the coating (effectively decreasing ASR). Observed ASR stability is possibly afforded by the oxygen diffusion-barrier properties of the amorphous Cr, Al oxide structure.

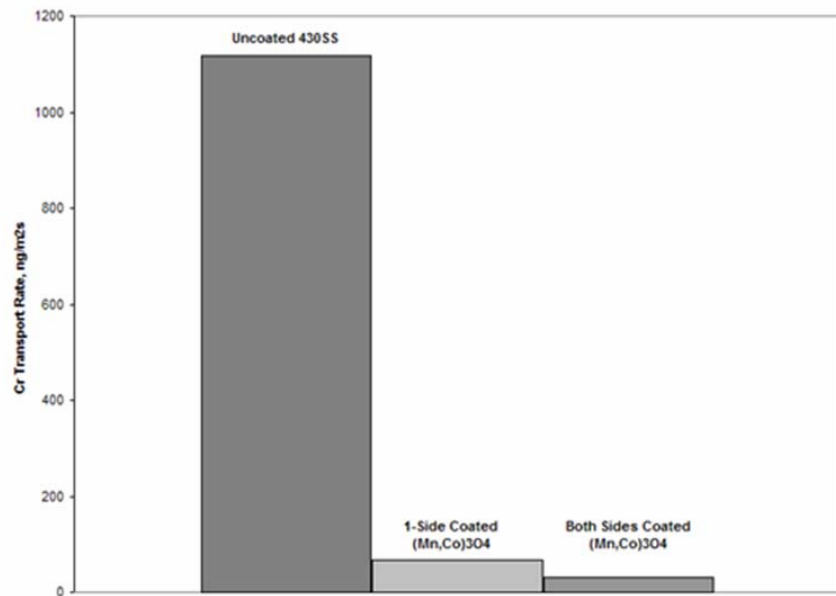
ASR for the LAFAD CoCrAlYO coated 430SS specimen decreases from  $>50\text{m}\Omega\cdot\text{cm}^2$  and stabilizes near  $\sim 30\text{m}\Omega\cdot\text{cm}^2$ . The lower ASR values compared with the LAFAD coatings without Co may be explained by the high conductivity of its oxides, e.g.,  $\text{CrCo}_2\text{O}_4$ , or  $\text{Co}_3\text{O}_4$ . Otherwise, regions of heterovalent Co may facilitate electron transport via hopping mechanisms. The initial ASR decrease may also be attributed to outward Mn transport from the 430SS, while its stability may be afforded by oxygen diffusion-barrier properties of the amorphous Cr, Al oxide matrix. The LAFAD TiCoMnCrAlYO coated 430SS exhibits the lowest ASR, which increases from  $<20\text{m}\Omega\cdot\text{cm}^2$  and stabilizes at  $\sim 20\text{m}\Omega\cdot\text{cm}^2$  during the first  $\sim 400$  hours (test ongoing). The initially low ASR may be due to the high Mn presence (15 at%) within the coating (Table

4.2a), which either forms conductive oxides, or an otherwise percolating network of heterovalent Mn regions in the amorphous coating. Depending upon long-term stability (ASR, chemical and microstructural), LAFAD TiCoMnCrAlYO coatings (or similar) may permit 430SS as an SOFC(IC) at 800°C.

### Cr Volatility

Figure 4.18 shows Cr volatility measurements (LBNL) at 800°C in moist air for 24 hours from three different 10 x 20 x 1mm 430SS specimens: one uncoated; one coated on one side with ~1µm FA-EBPVD  $(\text{Co},\text{Mn})_3\text{O}_4$ ; and, one coated on both sides with ~1µm FA-EBPVD  $(\text{Co},\text{Mn})_3\text{O}_4$ . The uncoated 430SS shows an average Cr transport rate of ~1100ng/m<sup>2</sup>s, the single-side coated specimen shows ~70ng/m<sup>2</sup>s and the specimen coated on both sides shows ~30ng/m<sup>2</sup>s. Dramatic reduction in Cr transport from both

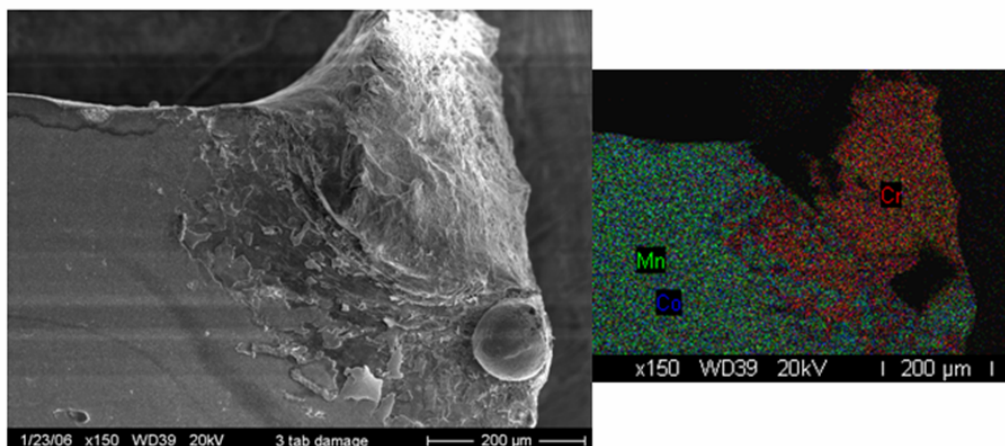
Figure 4.18. Cr volatility measurements (LBNL) from coated (FA-EBPVD  $(\text{Co},\text{Mn})_3\text{O}_4$ ) and uncoated 430SS.



coated samples is observed, and likely due to the absence of Cr within the near surface region. If the coatings completely blocked Cr volatility, one might expect a factor of 1/2 (Cr transport) from the specimen coated on only one side; however, instead a factor of ~1/16 is observed. SEM/EDS analyses revealed a substantial presence of Mn on the backside (uncoated) of the sample, which likely formed Cr-retaining  $(\text{Cr}, \text{Mn})_3\text{O}_4$ , effectively decreasing Cr volatility from the specimen backside [16,17]. During the FA-EBPVD process, ionized, multi-charged Mn species are likely very mobile in the plasma vapor/gas phase and adsorb on all surfaces. This may explain the significant Mn presence on the backside of the specimens transported via the ~0.5mm laser-cut space surrounding the tabbed coupons (Figure 3.1).

On both coated samples, remaining Cr transport is likely from small uncoated areas near the break-away tab from the laser cutting operation. Evidence for this is presented by the SEM/EDS image of the breakaway tab area in Figure 4.19. The tab area where the specimen was connected to the larger plate during the FA-EBPVD process was

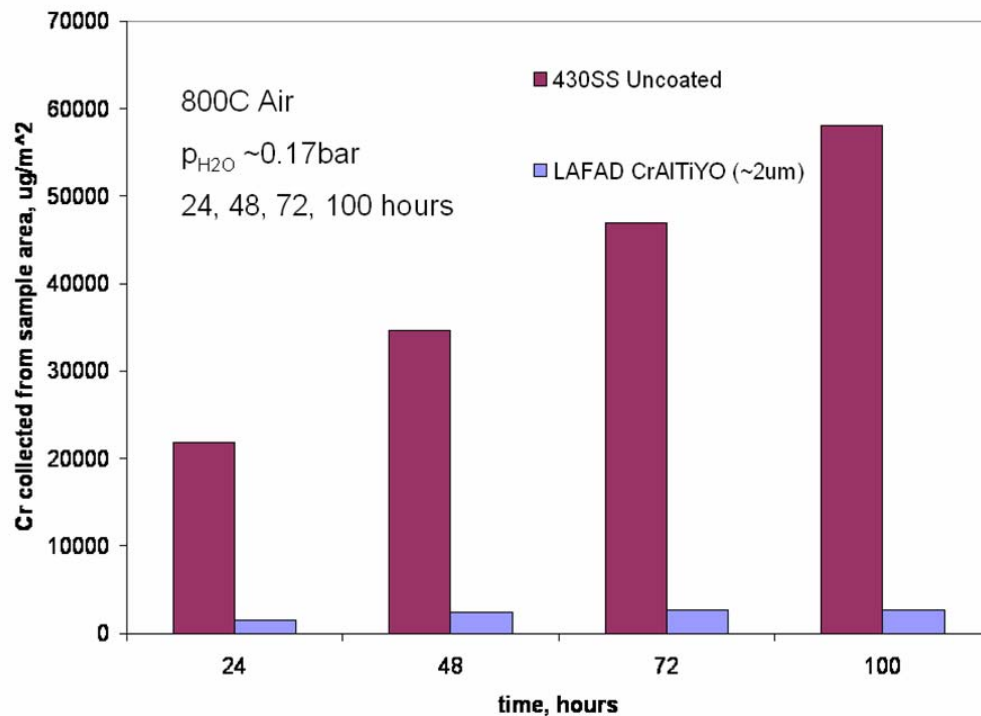
Figure 4.19. SEM image and EDS elemental mapping of specimen surface near breakaway tab area showing coating removal and substrate exposure.



exposed during specimen detachment. The detachment also resulted in localized removal of the CoMnO coating, and direct exposure of the underlying 430SS. After the oxidation process, the chromia-based scale is exposed and presumably contributes to the observed Cr vapor transport.

Figure 4.20 presents preliminary Cr volatility measurements (MSU) from coated and uncoated 430SS specimens (LAFAD TiCrAlYO coatings  $\sim 2\mu\text{m}$  on both sides). In this case, cumulative Cr amounts per specimen surface area are reported for  $\sim 24$  hour increments up to 100 hours. Compared with uncoated 430SS, a substantial Cr volatility reduction is observed in the LAFAD TiCrAlYO coated specimen. Cr volatility for the uncoated 430SS continues to increase, transporting  $>50,000\mu\text{g}/\text{m}^2$  from the specimen during the 100 hour test. This compares with  $<3,000\mu\text{g}/\text{m}^2$  from the coated specimen,

Figure 4.20. Cr volatility measurements (MSU) from coated (LAFAD TiCrAlYO) and uncoated 430SS.



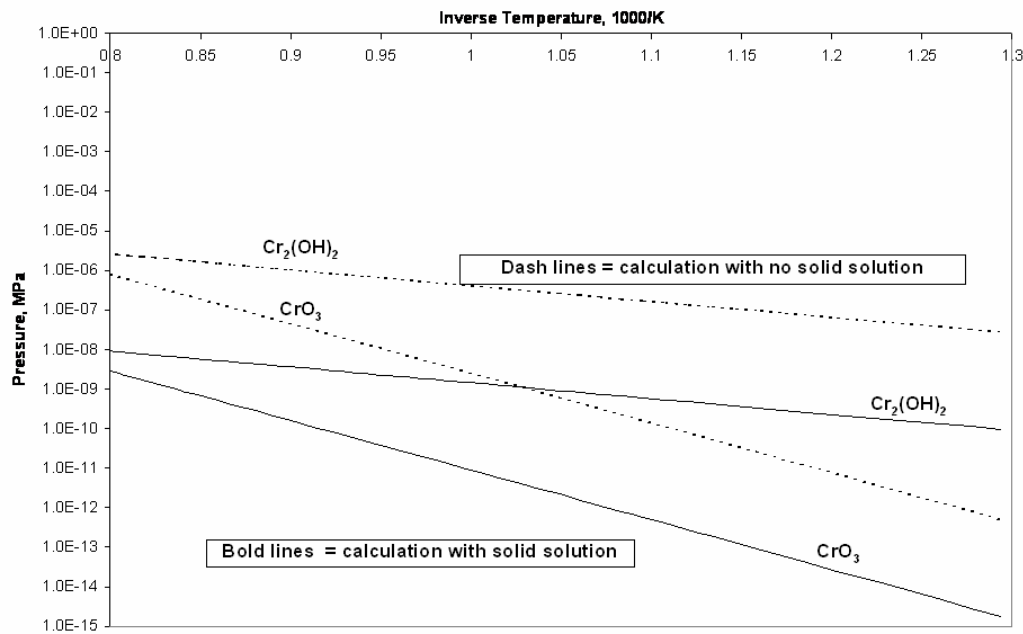
which was not observed to increase between ~72 and 100 hours into the test. The atomic percentage of Cr measured in the LAFAD TiCrAlYO is ~13 at% (Table 4.2), compared to ~30 at% within the TGO scale on uncoated 430SS. Therefore, the reduced total amount of surface Cr (available to form volatile Cr(VI) oxides) in the coating compared to the TGO scale does not fully explain the observed Cr volatility reduction.

Considering Equations 2.19 and 2.20, the thermodynamic activity of  $\text{Cr}_2\text{O}_3$ ,  $a_{\text{Cr}_2\text{O}_3}$ , must be significantly lower within the LAFAD TiCrAlYO coatings compared with  $\text{Cr}_2\text{O}_3$ -based TGO scales. This has been observed in other Cr containing oxides, e.g.,  $\text{LaCrO}_3$ , where the equilibrium vapor pressures of volatile Cr species are lower than would be predicted on the basis of Cr concentration alone [36]. For complex ceramic oxides lacking thermochemical data (e.g., amorphous/nano-crystalline LAFAD TiCrAlYO coatings) thermodynamic equilibrium modeling of Cr volatility can be approached via considerations of solid solutions, in which Gibbs free energy of a multiple component system is lower in a mixed state compared with that of the individual components [23].

Figure 4.21 illustrates calculated thermodynamic equilibrium vapor pressures of volatile Cr species (in moist air at different temperatures) above an oxide with elemental composition similar to that of the LAFAD TiCrAlYO coating. Calculations were made using TERRA thermodynamic equilibrium software, a recent development of the ASTRA code, which was developed by Prof. B.G. Trusov and used extensively for thermodynamic modeling in Eastern Europe during the 1980s-1990s [69]. The dashed line correlations represent calculations without ideal solid solution behavior assumption,

whereas the solid lines are those made with this assumption (all condensed-phase oxides in solid solution). Over an order of magnitude reduction in vapor pressures are estimated in the ideal solid solution scenario. This is due to reduced Gibbs free energy of the system with miscible phases compared with that of a mixture of independent immiscible phases. More accurate predictions of Cr volatility would likely result from consideration of regular and sub-regular solid solution models. Thermodynamic analysis helps to understand a possible basis for the substantial reduction of Cr volatility observed in Cr-containing LAFAD TiCrAlYO coatings compared to the  $\text{Cr}_2\text{O}_3$ -based TGO on 430SS.

Figure 4.21. Calculated thermodynamic equilibrium vapor pressures of Cr species (in moist air 800C air) above LAFAD TiCrAlYO coating.



## CHAPTER 5

## CONCLUSIONS

Summary Of Results

A wide variety of thin film ( $<5\mu\text{m}$ ) ceramic nitride, oxinitride and oxide protective coatings were deposited on ferritic steels using LAFAD and FA-EBPVD techniques. Permutations to the basic design included numerous coating stratigraphies and composite structures. Investigations are ongoing to understanding both basic characteristics and SOFC(IC)-relevant behaviors of these coatings. This thesis highlights significant results and discusses observations common among many of the coatings investigated. In general, it is concluded that LAFAD and FA-EBPVD hold promise for depositing protective coatings enabling the use of ferritic steel SOFC(IC)s at 800°C. This conclusion is based on the observed surface stability, low and stable ASR, and minimal Cr volatility exhibited by many of the LAFAD and FA-EBPVD coatings.

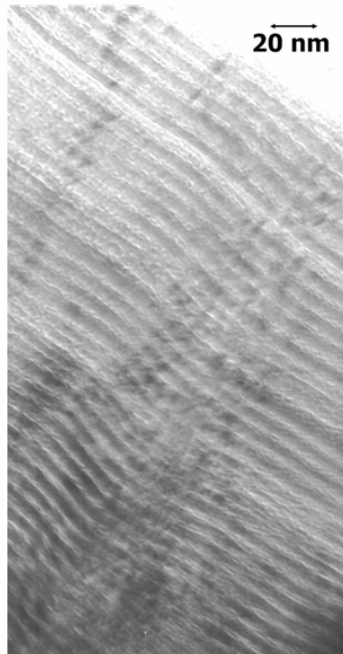
Deposition process parameters were engineered to produce combinations of favorable SOFC(IC) protective coating characteristics, e.g., thermal stability, diffusion-barrier properties, Cr-retention, and low ASR. Candidate SOFC(IC) coatings were identified, several of which are now being characterized using full-scale prototype SOFC(IC) geometries in operating stack conditions in collaboration with industrial and national laboratory SOFC development teams. Considerations for further evaluation of LAFAD and/or FA-EBPVD SOFC(IC) protective coatings, in addition to extension into similar high-temperature coating applications are discussed below.

### Considerations for Future Work

With promising LAFAD and/or FA-EBPVD coating compositions identified for the SOFC(IC) application, future work should involve a systems approach, exploring SOFC(IC) behavior in prototype conditions, and ultimately in stack operation. In this study, specimens were predominately subjected to 800°C air for various durations. Although this can effectively serve as an initial screening test, SOFC(IC)s in operation will be contacting anode, cathode and seal materials, in addition to being simultaneously exposed to anode and cathode gas phase environments, with thermal cycling events. Any complexities arising from these conditions must be characterized to facilitate appropriate materials engineering. Experimental apparatuses to simulate SOFC(IC) dual atmosphere and thermal cycling exposures are now in use at MSU. Experimental designs to elucidate materials interactions with SOFC cathodes and seals are being developed. While furthering the understanding of SOFC(IC) materials behavior through these experiments, a concurrent effort should be made to effectively transition the science into commercially-viable technologies. This effort should focus on scale-up designs to accommodate repeatability, high-throughput, and economic feasibility. In addition, considerations should be made for appropriate materials in non-cathode-contacting SOFC(IC) areas, such as sealing areas or at the surface of flow channels. Without electronic conductivity requirements, these areas may permit a wider selection of protective coatings. Different coatings could be applied to different areas via masking techniques common in the semi-conductor fabrication industry.

Various layered and single-segment LAFAD nitride and oxinitride coatings were initially explored in this study, many with promising SOFC(IC) attributes. An example TEM image of a LAFAD CrN/(CrN/AlN) layered coating is presented in Figure 5.1. Although some nitride and oxinitride coatings showed compositional stability during 800°C air exposures, long-term exposures (>40,000 hours) will likely favor oxide transformation, with any associated volumetric changes. The thermal stability of LAFAD nitride and oxinitride coatings should continue to be investigated, however, due to the favorable SOFC(IC) performance demonstrated by the LAFAD oxide coatings, nitride and oxinitride compositions may be superfluous for the SOFC(IC) application at 800°C.

Figure 5.1. TEM image of LAFAD CrN/(CrN/AlN) layered coating on 304 steel.



The thermal stability of layered LAFAD coating structures is also of continued interest, especially for applications involving mechanical criteria (e.g., wear or erosion resistance). In applications such as the SOFC(IC) at 800°C, however, layered structures may suffer three challenges: eventual homogenization, cost, and difficulties in maintaining layered structures over 3-D components (e.g., SOFC(IC) flow channels). It is for these reasons, LAFAD nano-composite amorphous/nano-crystalline ceramic oxide coatings of uniform composition may be favored for the SOFC(IC) application.

Of particular interest is the thermal stability of LAFAD amorphous/nano-crystalline composite coating structures. Future work may consider upper temperature limits of the observed stability, in addition to diffusion-barrier properties compared with their poly-crystalline counterparts having identical compositions. Extended applications for these types of structures may include thermal-barrier coating applications, in which diffusion-barrier properties dictate critical component durability (e.g., turbine vanes and blades). In addition to further investigating LAFAD and FA-EBPVD technologies for SOFC(IC) applications, this work may segue well into other (less-economically sensitive) high-temperature coating applications.

Applicability of LAFAD and/or FA-EBPVD SOFC(IC) protective coatings techniques ultimately lies in process economics. High capital costs associated with vacuum-based coating deposition technologies may restrict these techniques from full-scale SOFC(IC) protective coatings at high-volume production rates [8]; however, similar techniques have proven economical for other applications and further economic feasibility analyses are warranted. These techniques may find application in micro-SOFC

applications, where higher-quality coatings may be necessary and possibly used for fabricating other SOFC components, e.g., electrolytes [8]. The discovery of efficacious LAFAD and FA-EBPVD coating compositions and structures can also guide development of lower-cost deposition technologies (non-vacuum) that result in similar coating compositions and structures.

LAFAD and FA-EBPVD technologies have proven to be effective engineering tools for tailored synthesis of unique and functional thin film coatings. The inherent versatility in coating compositions and structures lends itself well to optimization of SOFC(IC) protective coatings, in addition to countless other thin film coating applications.

## REFERENCES CITED

1. Science and Technology of Ceramic Fuel Cells, Nguyen Q Minh and Takehiko Takahashi, Elsevier, 1995
2. High-temperature Solid Oxide Fuel Cells: Fundamentals, Design and Applications, Eds. Subhash C. Singhal and Kevin Kendall, Elsevier, 2003.
3. Fuel Cell Systems Explained, 2<sup>nd</sup> Edition, James Larminie and Andrew Dicks, Wiley 2003
4. Fuel Cell Handbook – 7<sup>th</sup> (2005) Edition US Department of Energy’s National Energy Technology Laboratory [www.netl.gov](http://www.netl.gov)
5. Williams MC *et al*, *Solid State Ionics* 177 (2006) 2039-2044
6. Sriramulu S *et al*, *The Fuel Cell Review*, Vol 3, Issue 2 (2006) 15-20
7. Williams MC *et al*, *Journal of Power Sources*, Vol 159, Issue 2 (2006) 1241-1247
8. Pederson LR *et al*, *Vacuum* 80 (2006) 1066–1083
9. Grove WR *Philosophical Magazine and Journal of Science*, 1843
10. Fuel Cell History Project, National Museum of American History Washington, DC 20560-0631 <http://americanhistory.si.edu/fuelcells/index.htm>
11. Fuel Cell Technologies: State and Perspectives, Eds. Nigel Sammes, Alevtina Smirnova and Oleksandr Vasylyev, Springer, 2005
12. Williams MC, Proceedings of the 7<sup>th</sup> International Symposium on Solid Oxide Fuel Cells, eds. S.C.Singhal and H.Yokakawa, pp. 3-7, The Electrochemical Society, Inc. Pennington, NJ (2003)
13. Zhu WZ *et al*, *Materials Science and Engineering A*, v 348, n 1-2, May 15, 2003, p 227-243
14. Yang Z *et al*, *J. Electrochem. Soc.* 150 (2003) A1188-A1201.
15. MSDS No. 8005 June, 2004 ThyssenKrupp VDM – Crofer 22 APU “High-temperature Alloy”
16. Yang Z *et al*, *J. Electrochem. Soc.* 151 (2004) pp. A1825-A1831

17. Gannon PE *et al*, *Int. J. of Hydrogen Energy* – in print (2006)
18. Hwang HJ *et al*, *J. Am. Ceramics Society* 88 [11] (2006) 3275-3278
19. Orlovskaya N *et al*, *J Am. Ceramics Society* 87 [10] (2004) 1981-1987
20. Lee EA *et al*, *Journal of Power Sources*, 157 (2006) 709-713.
21. Diffusion in Solids and High-temperature Oxidation of Metals, ed. Nowotny J, Trans Tech Publications, Ltd. 1992
22. Introduction to the High-Temperature Oxidation of Metals, 2<sup>nd</sup> Ed., Neil Birks, Gerald H. Meier and Fred S. Pettit, Cambridge University Press 2006
23. Introduction to Solid State Physics, Charles Kittel, John Wiley & Sons, Inc. 1996
24. The CRC Handbook of Solid State Electrochemistry, eds. Gellings PJ and Bouwmeester HJM, CRC Press 1997
25. Wagner C, *Z. Phys. Chem.*, 21 (1933) 25
26. Stinger J *Corrosion Science*, 1970 Vol. 10, pp. 513-543
27. Stott FH *Rep. Prog. Phys.* **50** (1987) 861-913. Printed in the UK
28. Opila E *J. Materials Science Forum* Vols. 461-464 (2004) 765-774
29. Gannon PE *et al*, *Surface and Coatings Technology* 188-189 (2004) 55-61
30. Gindorf C *et al*, Proceedings of the 4<sup>th</sup> European Solid Oxide Fuel Cell Forum July 10-14, 2000 Lucerne, Switzerland pp. 845-854
31. Yang Z *et al*, Ceramic engineering and science proceedings: Vol. 26 No. 4 (2005) pp. 217-223
32. Huczkowski P *et al*, *Materials and Corrosion*, (2004) 55, No. 11 pp. 825- 830
33. Handbook of Corrosion Engineering, Pierre R. Roberge, McGraw Hill 1999.
34. Gindorf C *et al*, *J. of Physics and Chemistry of Solids* V. 66 (2005) 384-387
35. Jiang SP *et al*, *J. of the European Ceramic Society* 22 (2002) 361-373

36. Hilpert K *et al*, *J. Electrochem. Soc.*, Vol. 143, No. 11, pp. 3642-3647 (1996)
37. Tucker M *et al*, *J. Power Sources*, Journal of Power Sources 160 (2006) 130–138
38. Chen X *et al*, *Solid State Ionics* 176 (2005) 425-433
39. Johnson C *et al*, *J. Electrochem. Soc.* Vol 2 (2005) 1842-1850.
40. Schiller G *et al*, *J. Advanced Materials*, vol 32 issue 1 (2000) 3-8.
41. Armstrong T J *et al*, SOFC-IX Proceedings (Electrochemical Society) 2005-07  
1795-1805
42. Przybylski K *et al*, *Materials Science Forum*, Vol 461 (2004) 1099-1106.
43. Konyshewa E *et al*, *Solid State Ionics* 177 (2006) 923-930.
44. Simner SP *et al*, *Ceramic Eng. and Sci. Proc.* Vol 26, No. 4 (2005) 83-90.
45. Quadakkers WJ *et al*, *Solid State Ionics* 91 (1996) 55-67.
46. Qu W *et al*, *J. Power Sources*, 138, (2004) 162-173.
47. Qu W *et al*, *J. Power Sources*, 153, (2006), 114-124.
48. Brylewski T. *et al*, *Materials Chemistry and Physics* 81 (2003) 434-437.
49. Kim JH *et al*, *Solid State Ionics* 174 (2004) 185-191
50. Larring Y *et al*, *J. Electrochem. Soc.*, 147, (9), (2000) 3251-3256.
51. Yang Z *et al*, *J. Electrochem. Soc.*, 152, (9) (2005) A1896-A1901.
52. Ceramic Films and Coatings, Eds. Wachtman JB, Haber RA, Noyes 1993
53. Thin Film Deposition: Principles and Practice, Donald L. Smith, McGraw-Hill 1995
54. Materials Science of Thin Films, 2<sup>nd</sup> ed. Milton Ohring, Academic Press 2002
55. Gorokhovsky VI *et al*, *Surface and Coatings Technology* 140 (2) (2001) 82
56. Gorokhovsky VI United States Patent No. 66637552
57. Gorokhovsky *et al*, *J. Electrochem. Soc.* 153 (10) A1886-A1893 (2006)

58. Gannon PE *et al*, *Surface and Coatings Technology*, submitted Aug. 2006
59. Smith RJ *et al*, *Journal of Materials Engineering and Performance*, v 13, n 3, June, 2004, p 295-302
60. Stevenson JW *et al*, presented at 7<sup>th</sup> Annual SECA Workshop and Peer Review, Philadelphia, PA, September 14, 2--6 7thAnnual SECA Workshop and Peer Review  
<http://www.netl.doe.gov/publications/proceedings/06/seca/pdf/Stevenson.PNL%20interconnects%20%26%20coatings.pdf>
61. Aukrust E, Muan A, *J. Amer. Ceram. Soc.* 1963 (46), 511
62. Iordanova N *et al*, *J. of Chem. Phys.* (123), 7, pp.074710-074710-11 (2005)
63. Elangovan S *et al*, *J. Mater. Eng. & Perform.* 2004, 13, pp. 265-273
64. Johnson C *et al*, *Composite Part B: Eng.*, 2004, 35, 167-172.
65. Abeilan JP *et al*, SOFC VII- Electrochem. Soc. Proc. PV-2001-16, eds., S.C. Singhal and M. Dokya, pp. 811-819, 2001, The Electrochemical Proceedings Series, Pennington, NJ
66. Quadakkers WJ, Shemet V, and Singheiser L, US Patent No. 2003059335, 2003.
67. Quadakkers WJ *et al*, Proc. 4<sup>th</sup> European SOFC Forum, vol. 2, pp. 827-836, 2000, European Fuel Cell Forum, Switzerland.
68. High-Temperature Oxidation of Metals, Per Kofstad, John Wiley & Sons, 1966
69. Vatolin NA, Moiseev GK, Trusov BG, Thermodynamic Modeling in High Temperature Inorganic Systems, Metallurgy, Moscow, 1994 (in Russian).